Available online at www.sciencedirect.com
SCIENCE DIRECT®
Comput. Methods Appl. Mech. Engrg. 195 (2006) 5198–5219
Computer methods in applied mechanics and engineering
www.elsevier.com/locate/cma

# 3D Crack propagation in unreinforced concrete. A two-step algorithm for tracking 3D crack paths

Thomas C. Gasser [a], Gerhard A. Holzapfel [a,b,*]

[a] Royal Institute of Technology (KTH), Department of Solid Mechanics, Osquars Backe 1, SE 100 44 Stockholm, Sweden
[b] Graz University of Technology, Institute for Structural Analysis, Computational Biomechanics, Schiesstattgasse 14-B, A-8010 Graz, Austria

Received 2 March 2005; received in revised form 26 October 2005; accepted 26 October 2005

**Abstract**

Tensile failure of unreinforced concrete involves progressive micro-cracking, and the related strain-softening can coalesce into geometrical discontinuities, which separate the material. Advanced mechanical theories and numerical schemes are required to efficiently and adequately represent crack propagation in 3D. In this paper we use the concept of strong discontinuities to model concrete failure. We introduce a cohesive fracture process zone, which is characterized by a transversely isotropic traction–separation law. We combine the cohesive crack concept with the partition of unity finite element method, where the finite element space is enhanced by the Heaviside function. The concept is implemented for tetrahedral elements and the failure initialization is based on the simple (non-local) Rankine criterion. For each element we assume the embedded discontinuity to be flat in the reference configuration, which leads to a non-smooth crack surfaces approximation in 3D, in general; different concepts for tracking non-planar cracks in 3D are reviewed. In addition, we propose a two-step algorithm for tracking the crack path, where a predictor step defines discontinuities according to the (non-local) failure criterion and a corrector step draws in non-local information of the existing discontinuities in order to predict a 'closed' 3D crack surface; implementation details are provided. The proposed framework is used to analyze the predictability of concrete failure by two benchmark examples, i.e. the *Nooru-Mohamed test*, and the *Brokenshire test*. We compare our numerical results, which are mesh independent, with experimental data and numerical results adopted from the literature.


*Keywords:* 3D crack propagation; Unreinforced concrete; Tracking algorithm; PUFEM

## 1. Introduction

Prevention of failure by fracture of structural components in service is a major concern in engineering (see, e.g., [1]). In particular, the study of structural failure of concrete has been of extensive academic and industrial importance in the past three decades.

At least since the findings in [20] we know that (classical) linear fracture mechanics of sharp cracks is an inadequate concept to be used for concrete structures, an assertion which has been supported by several other authors in the meanwhile. Tensile failure of unreinforced concrete involves progressive micro-cracking, debounding and other complex irreversible processes of internal damage. The associated strain-softening can coalesce into a geometrical discontinuity, which separates the material. Hence, the discrete crack concept is the approach that reflects this type of phenomena closest.

* Corresponding author. Address: Royal Institute of Technology (KTH), Department of Solid Mechanics, Osquars Backe 1, SE 100 44 Stockholm, Sweden. Tel.: +46 8 790 8205; fax: +46 8 411 2418.
*E-mail addresses:* gh@biomech.tu-graz.ac.at, gh@hallf.kth.se (G.A. Holzapfel).
*URL:* http://www.cis.tu-graz.ac.at/biomech (G.A. Holzapfel).

0045-7825/$ - see front matter © 2005 Elsevier B.V. All rights reserved.
doi:10.1016/j.cma.2005.10.023

Concrete may be considered as a quasi-brittle material, in which a sizeable nonlinear zone develops at the fracture front, which is almost entirely filled by the fracture process zone, and wherein plasticity effects are negligible [5]. Concrete failure shows pronounced strain-softening phenomena, and hence a description within polar (local) continuum mechanics fails (energy dissipated at failure is incorrectly predicted to zero [6]) and advanced theories are required.

Constitutive modeling of concrete failure has not yet resulted in the model, or the set of models, capable of representing the whole range of mechanical characteristics of concrete in a consistent and robust manner. Numerous constitutive models for concrete have been proposed in the past which are based on plasticity theories, fracture theories (fixed crack, rotating crack and multi-non-orthogonal fixed crack methods), damage theories and formulations which couple these approaches, see [16,17]. For comparative studies of 3D-constitutive models for concrete pointing out the diverging results, see, for example, [40].

One objective of the present work is the constitutive modeling of 3D crack propagation in unreinforced concrete for mixed mode situations, where, for a first approximation, fracture parameters for the opening mode (mode I) are used. This holds if the amount of shear stresses compared with tensile stresses is moderate, and hence shear friction and aggregate interlocking are negligible. In Section 2 we briefly review the needed continuum mechanical framework, the kinematics to capture concrete failure by means of strong discontinuities, the finite element formulation, and follow in Section 3 the pioneering works [11,4] for elasto-plastic fracture in metals, and [14] for quasi-brittle failure of concrete materials. We introduce a cohesive fracture process zone and employ a recently proposed transversely isotropic cohesive model [13], which is based on the theory of invariants [48]. It is suitable to describe the typical traction–separation behavior of tensile failure in concrete in a phenomenological way. For additional particularizations of Traction Separation Laws (TSLs), for example, for cubic, exponential and trilinear TSLs see [27,28,52]. More references utilizing the idea of cohesive zones to model material failure, and a general discussion on the limitations of cohesive models are provided in the seminal work [5]. Note that, alternatively, concrete failure may also be captured by means of weak discontinuities, where a jump is added to the strain field [37,7,24,47]. In [33] it is shown that a strong discontinuity problem may be regarded as a limiting case of a weak discontinuity problem as the width of the localization band tends to zero.

Another objective of the present work is the numerical modeling of 3D crack propagation in unreinforced concrete by employing the Partition of Unity Finite Element Method (PUFEM), which allows a treatment of the separation of a material in a very robust and efficient way (for details on the PUFEM see [25]). We enhance the finite element space by the Heaviside function according to [56], and combine the method with the cohesive crack concept. This leads to a finite element formulation with embedded strong discontinuities, which has several advantages over traditional smeared and discrete approaches (see, for example, [19,23]). It is worth noting that, alternatively, strong discontinuities have been combined with finite element formulations, which are based on the mixed Enhanced Assumed Strain (EAS) method, as proposed in [45]. EAS-methods for the geometrically linear regime are presented in [44,2,31,55], while [3,49] extend the concept to the nonlinear regime. A comparative study of the formulations based on the EAS concept was recently presented in the authors' work [12]. Therein we concluded that either the three-field Hu–Washizu variational formulation or the kinematics of strong discontinuities are satisfied, but not both together, which may lead to not meaningful numerical results for the separation process governed by, for example, stress locking phenomena.

The fully 3D PUFEM implementation is based on two variational statements arising from a standard single-field variational formulation in spatial description. The numerical model has been utilized for tetrahedral elements using the multipurpose finite element analysis program FEAP [51]. A critical task for applying the PUFEM to 3D is the representation of the crack surface. We assume that the embedded discontinuity within a particular finite element is a flat surface in the reference configuration (for details see [13]), therefore, the proposed concept leads, in general, to a non-smooth crack surface in 3D. In Section 4 we discuss different concepts for representing non-planar crack surfaces in 3D documented in the literature. Perhaps the most popular approaches is the Level Set Method (LSM) [50,26] (originally proposed in [38]), and a global tracking algorithm which is based on the solution of a kind of 'heat conduction' problem [35]. Recently, however, the study in [54] claims that the standard LSM is not an ideal solution for characterizing cracks, while the algorithm proposed in [35] requires the solution of a 'thermal-like' problem before each mechanical loading step, which is related to high computational cost. Hence, in Section 5 we describe in detail a two-step algorithm for tracking multiple non-planar cracks in 3D, which is fundamentally different from the above mentioned approaches. The first step, the predictor say, can be seen as a generalization of a (simple) local strategy of tracking 2D strong discontinuities, documented in [55], to 3D. The second step, the corrector say, draws in non-local information of the existing discontinuities in order to predict a 'closed' 3D crack surface. The proposed non-local smoothing strategy effectively circumvents topological difficulties, which may arise from the predictor step. Details about the implementation of the algorithm for tracking the 3D crack path are provided. The proposed computational framework, which combines PUFEM with the new smoothing algorithm for non-planar 3D cracks, is now used to analyze the predictability of concrete failure by means of two representative numerical examples, i.e. the *Nooru-Mohamed test*, a mixed mode failure test, and the *Brokenshire test*, a torsion failure test. The objective is to present the robustness and efficiency of the proposed framework. The computational results are documented in Section 6, and compared with experimental and numerical data adopted from the literature.

## 2. Continuum mechanical framework, strong discontinuity

In this section we briefly provide an overview of the continuum mechanical framework and the kinematics of strong discontinuities necessary for this work (for a more detailed account see, for example, [30,15,13]). In addition to the standard kinematical description in continuum mechanics, the *Heaviside* function is introduced in order to represent a strong discontinuity. The application of a single-field variational principle to that kinematical description gives two variational statements, which form the basis for the finite element implementation. Finally, the strong discontinuity is represented by addition nodal degrees of freedom, and the related finite element representation falls into the class of the PUFEM [25].

### 2.1. Kinematics

In order to elaborate on the kinematics we consider the reference configuration $\Omega_0$ of a body. In $\Omega_0$ a discontinuity $\partial\Omega_{0\,\mathrm{d}}$ is embedded and separates the body into two sub-domains occupying two sub-domains $\Omega_{0+}$ and $\Omega_{0-}$. A deformation $\boldsymbol{\chi}(\mathbf{X})$, applied to the reference configuration, maps $\Omega_{0+}$ and $\Omega_{0-}$ into their current configurations $\Omega_+$ and $\Omega_-$, where $\mathbf{X}$ denotes the referential position of a material point. Thereto, the kinematics of the separation is represented by means of a strong discontinuity in the displacement field, i.e. $\mathbf{u}(\mathbf{X}) = \mathbf{u}_{\mathrm{c}}(\mathbf{X}) + \mathscr{H}(\mathbf{X})\mathbf{u}_{\mathrm{e}}(\mathbf{X})$, where $\mathscr{H}$ denotes the *Heaviside* function with the value 0 for $\mathbf{X} \in \Omega_{0-}$ and 1 for $\mathbf{X} \in \Omega_{0+}$. The additive decomposition of $\mathbf{u}$ is based on the introduction of the smooth fields $\mathbf{u}_{\mathrm{c}}$ and $\mathscr{H}\mathbf{u}_{\mathrm{e}}$ characterizing the compatible and the enhanced displacements, respectively.

Subsequently, the material gradient of the displacement field reads, with the property $\mathrm{Grad}\,\mathscr{H}(\mathbf{X}) = \delta_{\mathrm{d}}\mathbf{N}(\mathbf{X}_{\mathrm{d}})$ of the *Heaviside* function,

$$\mathrm{Grad}\,\mathbf{u}(\mathbf{X}) = \mathrm{Grad}\,\mathbf{u}_{\mathrm{c}}(\mathbf{X}) + \mathscr{H}\,\mathrm{Grad}\,\mathbf{u}_{\mathrm{e}}(\mathbf{X}) + \delta_{\mathrm{d}}(\mathbf{X})\mathbf{u}_{\mathrm{e}}(\mathbf{X}) \otimes \mathbf{N}(\mathbf{X}_{\mathrm{d}}), \tag{1}$$

where $\delta_{\mathrm{d}}$ denotes the *Dirac-delta* functional with the value 0 for $\mathbf{X} \notin \partial\Omega_{0\,\mathrm{d}}$ and $\infty$ for $\mathbf{X} \in \partial\Omega_{0\,\mathrm{d}}$. In addition, the material gradient operator is denoted by $\mathrm{Grad}(\bullet) = \partial(\bullet)/\partial\mathbf{X}$, and the unit normal vector $\mathbf{N}(\mathbf{X}_{\mathrm{d}})$ defines the orientation at an arbitrary (referential) point $\mathbf{X}_{\mathrm{d}} \in \partial\Omega_{0\,\mathrm{d}}$ of the discontinuity.

Based on (1) the deformation gradient is defined to be $\mathbf{F}(\mathbf{X}) = \mathbf{I} + \mathrm{Grad}\,\mathbf{u}(\mathbf{X})$, which serves the basis for computing appropriate strain tensors. Note that for a finite element representation of the discontinuous kinematics it is convenient to consider, for example, separate deformation gradients for the two sub-domains, i.e. an compatible deformation gradient $\mathbf{F}_{\mathrm{c}} = \mathbf{I} + \mathrm{Grad}\,\mathbf{u}_{\mathrm{c}}$ (with $\det\mathbf{F}_{\mathrm{c}} = J_{\mathrm{c}} > 0$), which maps $\Omega_{0-}$ into $\Omega_-$, and an enhanced deformation gradient $\mathbf{F}_{\mathrm{e}} = \mathbf{I} + \mathrm{Grad}\,\mathbf{u}_{\mathrm{c}} + \mathrm{Grad}\,\mathbf{u}_{\mathrm{e}}$ (with $\det\mathbf{F}_{\mathrm{e}} = J_{\mathrm{e}} > 0$), which maps $\Omega_{0+}$ into $\Omega_+$. For a constitutive representation of the separation of a material body by means of a cohesive zone model we assume a *fictitious* discontinuity $\partial\Omega_{\mathrm{d}}$, i.e. the map of $\partial\Omega_{0\,\mathrm{d}}$ to the related current configuration. Following [56], $\partial\Omega_{\mathrm{d}}$ is defined via the average deformation gradient $\mathbf{F}_{\mathrm{d}}(\mathbf{X}_{\mathrm{d}}) = \mathbf{I} + \mathrm{Grad}\,\mathbf{u}_{\mathrm{c}} + \mathbf{u}_{\mathrm{e}} \otimes \mathbf{N}/2$, with $\det\mathbf{F}_{\mathrm{d}} = J_{\mathrm{d}} > 0$, where the factor 1/2 enforces $\partial\Omega_{\mathrm{d}}$ to be placed in the middle between the two (physical) surfaces created by the crack formation. The idea of a mean surface of the cohesive zone was introduced in [53]. Based on $\mathbf{F}_{\mathrm{d}}$ the related unit normal vector $\mathbf{n} = \mathbf{N}\mathbf{F}_{\mathrm{d}}^{-1}/|\mathbf{N}\mathbf{F}_{\mathrm{d}}^{-1}|$ onto the fictitious discontinuity is then obtained by a weighted push-forward operation of the covariant vector $\mathbf{N}$.

### 2.2. Variational formulation

Point of departure is a standard single-field variational principle, where for simplicity inertia effects are neglect. Hence, $\int_{\Omega_0} \mathrm{Grad}\,\delta\mathbf{u} : \mathbf{P}(\mathbf{F})\,\mathrm{d}V - \delta\Pi^{\mathrm{ext}}(\delta\mathbf{u}) = 0$ holds, where $\mathbf{P}(\mathbf{F})$ and $\delta\mathbf{u}$ denote the first Piola–Kirchhoff stress tensor and the admissible variation of the displacement field, respectively. Subsequently, we assume dead loadings and define the admissible variation $\delta\mathbf{u} = \delta\mathbf{u}_{\mathrm{c}} + \mathscr{H}\delta\mathbf{u}_{\mathrm{e}}$ according to the introduced additive split of the displacement field $\mathbf{u}$. By using a push-forward operation the above introduced single-field variational principle gives the two spatial variational statements [13]

$$\left.\begin{aligned} &\int_{\Omega_-} \mathrm{sym}(\mathrm{grad}_{\mathrm{c}}\delta\mathbf{u}_{\mathrm{c}}) : \boldsymbol{\sigma}_{\mathrm{c}}\,\mathrm{d}v + \int_{\Omega_+} \mathrm{sym}(\mathrm{grad}_{\mathrm{e}}\delta\mathbf{u}_{\mathrm{c}}) : \boldsymbol{\sigma}_{\mathrm{e}}\,\mathrm{d}v - \delta\Pi_{\mathrm{c}}^{\mathrm{ext}}(\delta\mathbf{u}_{\mathrm{c}}) = 0, \\ &\int_{\Omega_+} \mathrm{sym}(\mathrm{grad}_{\mathrm{e}}\delta\mathbf{u}_{\mathrm{e}}) : \boldsymbol{\sigma}_{\mathrm{e}}\,\mathrm{d}v + \int_{\partial\Omega_{\mathrm{d}}} \mathbf{t}\cdot\delta\mathbf{u}_{\mathrm{e}}\,\mathrm{d}s - \delta\Pi_{\mathrm{e}}^{\mathrm{ext}}(\delta\mathbf{u}_{\mathrm{e}}) = 0, \end{aligned}\right\} \tag{2}$$

where $\mathrm{d}v$ is the infinitesimal volume element defined in the current configuration and $\mathrm{d}s$ is the infinitesimal surface element defined on the discontinuity $\partial\Omega_{\mathrm{d}}$. Moreover, $\boldsymbol{\sigma}_{\mathrm{c}} = J_{\mathrm{c}}^{-1}\mathbf{P}(\mathbf{F}_{\mathrm{c}})\mathbf{F}_{\mathrm{c}}^{\mathrm{T}}$ and $\boldsymbol{\sigma}_{\mathrm{e}} = J_{\mathrm{e}}^{-1}\mathbf{P}(\mathbf{F}_{\mathrm{e}})\mathbf{F}_{\mathrm{e}}^{\mathrm{T}}$ denote Cauchy stress tensors and $\mathbf{t}$ characterizes the Cauchy traction vector acting on the fictitious discontinuity $\partial\Omega_{\mathrm{d}}$. Contributions due to external loading are summarized in terms of the virtual external potential energies $\delta\Pi_{\mathrm{c}}^{\mathrm{ext}}$ and $\delta\Pi_{\mathrm{e}}^{\mathrm{ext}}$, which refer to the domains $\Omega_{0-}$ and $\Omega_{0+}$, respectively. The spatial gradients in (2) are defined according to $\mathrm{grad}_{\mathrm{c}}(\bullet) = \mathrm{Grad}(\bullet)\mathbf{F}_{\mathrm{c}}^{-1}$, $\mathrm{grad}_{\mathrm{e}}(\bullet) = \mathrm{Grad}(\bullet)\mathbf{F}_{\mathrm{e}}^{-1}$ and the operator $\mathrm{sym}(\bullet) = [(\bullet) + (\bullet)^{\mathrm{T}}]/2$ furnishes the symmetric part of $(\bullet)$.

The two variational statements (2) and the associated consistent linearization, as it is explicitly documented in [13], form the basis for the finite element implementation.

### 2.3. Finite element representation

The finite element implementation of (2) is used within PUFEM using the basic idea to enrich the interpolation functions such that they have good local approximation properties [25]. In our case we enrich the standard polynomial interpolation functions by the *Heaviside* function.

According to PUFEM, the displacement field $\underline{\mathbf{u}}$ can then be expressed as[1]

$$\underline{\mathbf{u}} = \sum_{i=1}^{n_{\text{elem}}} N^I \underline{\mathbf{u}}_{I\text{c}} + \mathscr{H} \sum_{i=1}^{n_{\text{elem}}} N^I \underline{\mathbf{u}}_{I\text{e}}, \tag{3}$$

where $N^I$ are the standard (polynomial) interpolation functions, and $I$ is an index running between 1 and the total number of element nodes, denoted by $n_{\text{elem}}$. In (3) regular and enhanced nodal displacements (degrees of freedom) are denoted by $\underline{\mathbf{u}}_{I\text{c}}$ and $\underline{\mathbf{u}}_{I\text{e}}$, respectively.

With use of (3) the two spatial variational statements (2) lead to the following linearized algebraic set of equations for a particular finite element $e$

$$\begin{bmatrix} \underline{\mathbf{K}}_{\mathbf{u}_\text{c}\mathbf{u}_\text{c}} & \underline{\mathbf{K}}_{\mathbf{u}_\text{c}\mathbf{u}_\text{e}} \\ \underline{\mathbf{K}}_{\mathbf{u}_\text{e}\mathbf{u}_\text{c}} & \underline{\mathbf{K}}_{\mathbf{u}_\text{e}\mathbf{u}_\text{e}} \end{bmatrix}^e_{i-1} \begin{bmatrix} \Delta\underline{\mathbf{u}}_\text{c} \\ \Delta\underline{\mathbf{u}}_\text{e} \end{bmatrix}^e_i = \begin{bmatrix} \underline{\mathbf{f}}^{\text{ext}}_{\mathbf{u}_\text{c}} \\ \underline{\mathbf{f}}^{\text{ext}}_{\mathbf{u}_\text{e}} \end{bmatrix}^e_{i-1} - \begin{bmatrix} \underline{\mathbf{f}}^{\text{int}}_{\mathbf{u}_\text{c}} \\ \underline{\mathbf{f}}^{\text{int}}_{\mathbf{u}_\text{e}} \end{bmatrix}^e_{i-1}, \tag{4}$$

where $i$, $i-1$ and $\Delta\underline{\mathbf{u}}_\text{c}$, $\Delta\underline{\mathbf{u}}_\text{e}$ denote the iteration steps associated with a global Newton iteration procedure, and the increments of the compatible and enhanced displacements, respectively.

In (4) the force vectors $\underline{\mathbf{f}}^{\text{ext}}_{\mathbf{u}_\text{c}}$, $\underline{\mathbf{f}}^{\text{ext}}_{\mathbf{u}_\text{e}}$ and $\underline{\mathbf{f}}^{\text{int}}_{\mathbf{u}_\text{c}}$, $\underline{\mathbf{f}}^{\text{int}}_{\mathbf{u}_\text{e}}$ denote nodal force vectors due to external and internal loadings, whereas the subscripts $(\bullet)_{\mathbf{u}_\text{c}}$ and $(\bullet)_{\mathbf{u}_\text{e}}$ denote their association with compatible and enhanced degrees of freedom, respectively. According to (2), the internal nodal force vectors read

$$\underline{\mathbf{f}}^{\text{int}}_{\mathbf{u}_\text{c}} = [\underline{\mathbf{f}}^{\text{int}\,1}_{\mathbf{u}_\text{c}}, \ldots, \underline{\mathbf{f}}^{\text{int}\,n_{\text{elem}}}_{\mathbf{u}_\text{c}}]^{\text{T}}, \quad \underline{\mathbf{f}}^{\text{int}\,I}_{\mathbf{u}_\text{c}} = \int_{\Omega^e_-} \underline{\mathbf{B}}^{I\text{T}}_\text{c} \underline{\boldsymbol{\sigma}}_\text{c}\, \text{d}v + \int_{\Omega^e_+} \underline{\mathbf{B}}^{I\text{T}}_\text{e} \underline{\boldsymbol{\sigma}}_\text{e}\, \text{d}v, \tag{5}$$

$$\underline{\mathbf{f}}^{\text{int}}_{\mathbf{u}_\text{e}} = [\underline{\mathbf{f}}^{\text{int}\,1}_{\mathbf{u}_\text{e}}, \ldots, \underline{\mathbf{f}}^{\text{int}\,n_{\text{elem}}}_{\mathbf{u}_\text{e}}]^{\text{T}}, \quad \underline{\mathbf{f}}^{\text{int}\,I}_{\mathbf{u}_\text{e}} = \int_{\Omega^e_+} \underline{\mathbf{B}}^{I\text{T}}_\text{e} \underline{\boldsymbol{\sigma}}_\text{e}\, \text{d}v + \int_{\partial\Omega^e_\text{d}} \underline{\mathbf{N}}^{I\text{T}} \underline{\mathbf{t}}\, \text{d}s, \tag{6}$$

where the $n_{\text{ndm}}$-dimensional sub-vectors $\underline{\mathbf{f}}^{\text{int}\,I}_{\mathbf{u}_\text{c}}$ and $\underline{\mathbf{f}}^{\text{int}\,I}_{\mathbf{u}_\text{e}}$ are related to the $I$th finite element node ($n_{\text{ndm}} = 3$ in our case). In addition, the quantities $\underline{\boldsymbol{\sigma}}_\text{c}$, $\underline{\boldsymbol{\sigma}}_\text{e}$ and $\underline{\mathbf{t}}$ represent the Voigt notation of the Cauchy stress tensors $\boldsymbol{\sigma}_\text{c}$, $\boldsymbol{\sigma}_\text{e}$ and the spatial traction vector $\mathbf{t}$. The symmetric gradient operators $\underline{\mathbf{B}}_\text{c}(\bullet) = \text{sym}[\text{grad}_\text{c}(\bullet)]$ and $\underline{\mathbf{B}}_\text{e}(\bullet) = \text{sym}[\text{grad}_\text{e}(\bullet)]$ are defined through the symmetric parts of the spatial gradients $\text{grad}_\text{c}(\bullet)$ and $\text{grad}_\text{e}(\bullet)$, respectively. Note that $\underline{\mathbf{B}}_\text{c}(\bullet)$, $\underline{\mathbf{B}}_\text{e}(\bullet)$ are related to the spatial configuration, hence they are sparsely filled, see, for example, [57].

The stiffness matrices $\underline{\mathbf{K}}_{\mathbf{u}_\text{c}\mathbf{u}_\text{c}}$, $\underline{\mathbf{K}}_{\mathbf{u}_\text{c}\mathbf{u}_\text{e}}$, $\underline{\mathbf{K}}_{\mathbf{u}_\text{e}\mathbf{u}_\text{c}}$, $\underline{\mathbf{K}}_{\mathbf{u}_\text{e}\mathbf{u}_\text{e}}$ in (4) are defined due to a consistent linearization of the internal loading vectors with respect to the compatible and enhanced displacements (for details see [13]). It is worth noting that, in general, the cohesive traction term $\int_{\partial\Omega^e_\text{d}} \underline{\mathbf{N}}^{I\text{T}} \underline{\mathbf{t}}\, \text{d}s$ in $(6)_4$ contributes not only to the stiffness matrix $\underline{\mathbf{K}}_{\mathbf{u}_\text{e}\mathbf{u}_\text{e}}$ but also to $\underline{\mathbf{K}}_{\mathbf{u}_\text{e}\mathbf{u}_\text{c}}$ [12,13].

## 3. Constitutive formulation

The reliability of numerical simulations of failure in concrete structures strongly depends on the employed constitutive formulations. In particular, under 3D loading conditions, constitutive models which are available in the literature predict sometimes significantly different results, as, for example, for the double-edge-notched specimen (DENS) applied to tensile and shear loadings (see [40]).

We assume the existence of a cohesive fracture process zone, in which initialization and coalescence of micro-cracks are lumped in terms of accumulation of damage, and, accordingly, in which high strain gradients prevail. Hence, the proposed approach requires two constitutive models, i.e. a continuous (bulk) material model, characterizing the material response of the bulk material, and a discontinuous (cohesive) material model, characterizing the material response of the cohesive zone. Note, however, that it was recently shown that every continuum constitutive model linked to strong discontinuity kinematics includes a discrete model in a consistent manner [32,36]. Nevertheless, we follow the more classical approach and assume a more or less ad hoc definition of the cohesive material model independently from the bulk material, and employ a (discrete) constitutive description of the cohesive zone recently introduced in [13]. From the practical point of view this approach turns out to be sometimes advantageous since one gets more flexibility in fitting experimental data.

[1] Characters indicated by underlines denote the matrix notation of the associated tensor or vector. For example, $\underline{\mathbf{u}}$ is the matrix representation of vector $\mathbf{u}$.

### 3.1. Bulk material response

We restrict our attention to concrete mainly under tensile loading. Hence, the continuous response may be modeled by a neo-Hookean material with the strain-energy function $\Psi(\mathbf{C})$ in the uncoupled form

$$\Psi(\mathbf{C}) = \kappa(\ln J)^2 + \frac{\mu}{2}(\overline{I}_1 - 3), \tag{7}$$

where $\kappa$ denotes the bulk modulus and $\mu$ the shear modulus of the bulk material. In (7) $\overline{I}_1 = \mathrm{tr}(\overline{\mathbf{C}})$ is the first invariant of the modified right Cauchy–Green tensor $\overline{\mathbf{C}} = J^{-2/3}\mathbf{C}$, where $\mathbf{C} = \mathbf{F}^{\mathrm{T}}\mathbf{F}$.

Standard derivations lead to the Cauchy stress $\boldsymbol{\sigma} = 2J^{-1}\mathbf{b}\partial\Psi/\partial\mathbf{b}$ and the associated spatial elasticity tensor $\mathbb{c} = 4J^{-1}\mathbf{b}(\partial^2\Psi/\partial\mathbf{b}\partial\mathbf{b})\mathbf{b}$, where $\mathbf{b} = \mathbf{F}\mathbf{F}^{\mathrm{T}}$ is the left Cauchy–Green tensor. For further details regarding the neo-Hookean material, see, for example, [15].

### 3.2. Cohesive material response

The cohesive (or discontinuous) material response is determined by an ad hoc definition of a traction separation law, which is governed by a number of material-dependent mechanisms such as cohesion at the atomistic scale, bridging ligaments, interlocking of grains and others in a phenomenological sense. In this section we briefly review a formulation of a transversely isotropic cohesive model, which satisfies the thermodynamic restrictions imposed on the second law of thermodynamics (namely the non-negativeness of the internal dissipation) for any thermodynamic process [13].

The cohesive model is based on the theory of invariants [48]. A cohesive potential of the form $\psi = \psi(\mathbf{u}_e \otimes \mathbf{u}_e, \mathbf{n} \otimes \mathbf{n}, \delta)$ is assumed, where the transversely isotropic structure is determined by the structural tensor $\mathbf{n}\otimes\mathbf{n}$, and the state of damage is represented by a single scalar internal variable $\delta \in [0, \infty[$ [12]. Recall that the unit normal vector $\mathbf{n}$ onto the fictitious discontinuity $\partial\Omega_d$ determines the preferred direction at an arbitrary (spatial) point (see Section 2.1). Following [48], the cohesive potential reads $\psi = \psi(i_1, i_2, i_3, i_4, i_5, \delta)$, where $i_1, \ldots, i_5$ are invariants, which depend on the symmetric tensors $\mathbf{u}_e \otimes \mathbf{u}_e$, and $\mathbf{n} \otimes \mathbf{n}$. In order to particularize the cohesive potential suitable to describe tensile failure of concrete, we assume

$$\psi(i_1, i_4, \delta) = \frac{t_0}{2\delta}\exp(-a\delta^b)[i_4 + \alpha(i_1 - i_4)], \tag{8}$$

where $t_0$ (cohesive tensile strength), $a$, $b$ and $\alpha$ (anisotropy parameter) are non-negative material parameters to be determined from experimental data. In particular $\alpha$ denotes the ratio between the transverse and normal stiffness of the cohesive zone ($\alpha = 1$ is for the isotropic case). In order to complete we define a damage surface $\phi(\mathbf{u}_e, \delta) = |\mathbf{u}_e| - \delta = 0$ in the three-dimensional enhanced displacement space and assume $\dot{\delta} = \overline{|\mathbf{u}_e|}$ for the evolution of the internal (damage) variable $\delta$. Based on the procedure by Coleman and Noll [10] the cohesive TSL takes on the form $\mathbf{t} = \partial\psi/\partial\mathbf{u}_e$, which is straightforward to derive from (8). For a subsequent finite element implementation, which uses the linearized constitutive equations, it is convenient to introduce $\mathbf{c}_{\mathbf{u}_e} = \partial\mathbf{t}/\partial\mathbf{u}_e$, $\mathbf{c}_{\mathbf{n}} = \partial\mathbf{t}/\partial\mathbf{n}$, $\mathbf{c}_\delta = \partial\mathbf{t}/\partial\delta$, representing the stiffness of the cohesive zone with respect to changes in the gap displacement $\mathbf{u}_e$, the orientation $\mathbf{n}$, and the state of damage characterized by $\delta$, respectively.

### 3.3. Failure criterion

It is well known that strain-softening in rate-independent constitutive models can lead to strain-localization instability and ('pathological') mesh-dependent solutions through a local material bifurcation. A necessary condition for strain localization is the singularity of the acustic tensor $\mathbf{Q}$, i.e.

$$\det \mathbf{Q}(\mathbf{n}) = 0, \quad \mathbf{Q} = \mathbf{n}\mathbb{c}\mathbf{n}, \quad Q_{ij} = c_{aijb}n_a n_b, \tag{9}$$

where $\mathbf{n}$ denotes the normal to the localization in the current configuration. Condition $(9)_1$ states that material stability is violated in the Mandel-sense [21], and acceleration waves cannot propagate through the solid at finite speed at every direction. We emphasize that the condition $\det\mathbf{Q} = 0$ is necessary but not sufficient for material instability, and several other conditions are discussed in the literature such as positive definiteness/singularity of the constitutive operator, strong ellipticity, flutter etc. (see, e.g., [8]). Note that the evaluation of the singularity of the acustic tensor provides information about (i) the initialization of the localization, and (ii) the orientation of the localization. Both informations are necessary when utilizing a crack path tracking algorithm.

Although the above concept of localization is well-established, frequently applied, and extensively documented in the literature, (see, for example [42]), its application to general boundary-value problems within a numerical framework may be associated with high computational cost. Note that for complex material models, for which, in general, no analytical expressions for the elasticity tensor $\mathbb{c}$ in the spatial description are available, the computation of the orientation $\mathbf{n}$ of the failure surface can be difficult. In particular for unreinforced concrete, easier concepts are available. For example, the

*Rankine* criterion seems to provide sufficient accuracy. Thereby, the initialization of the failure is achieved when the maximum principal Cauchy stress $\sigma_{\max}$ exceeds a material-dependent stress limit. Moreover, the orientation $\mathbf{n}$ of the failure may simply be determined by the direction of the maximum principal stress. Hence, at a spatial point $\mathbf{x}$ one has simply to solve the eigenvalue problem

$$(\boldsymbol{\sigma}(\mathbf{x}) - \lambda_i \mathbf{I})\mathbf{v}_i = \mathbf{0}, \quad \text{no summation over } i, \tag{10}$$

where $\lambda_i$ and $\mathbf{v}_i$ are the $n_{\text{dim}}$ eigenvalues and eigenvectors, respectively. Finally, we define $\sigma_{\max} = \lambda_1$ as the largest eigenvalue and the related eigenvector as $\mathbf{n} = \mathbf{v}_1$.

The main advantage of the *Rankine* criterion over the localization criterion, which is based on the singularity of the acustic tensor, is its simplicity. Despite of that it is well known that tensile-dominated failure of concrete causes zones of small volume, where accumulation of damage and other inelastic effects are present, while the main portion of the material deforms purely elastic. Thus, the coupling of the elastic bulk material with the inelastic cohesive zone, as proposed in this work, is a natural modeling assumption. It is a simple way of capturing the physical phenomena and it avoids the introduction of damage-based softening of the bulk material.

Finally note that the relations (9) and (10) are related to the current configuration, whereby the crack path tracking algorithm, as discussed in Section 5, works in the reference configuration, hence a *pull back* of the spatial normal vector $\mathbf{n}$ to the referential configuration is required in order to obtain $\mathbf{N} = \mathbf{nF}/|\mathbf{nF}|$.

#### 3.3.1. Implementation of the failure criterion

Numerical examples show that Eq. (10) cannot be used on an element level to characterize the propagation of the failure zone (discontinuity) since a highly scattered normal vector field evolves. This has been observed even for 2D problems by using triangular finite elements [55]. Since it is obvious that a scattered normal vector field cannot be used for a representation of the failure zone, a non-local smoothing of the normal vector field has been proposed [55,13]. In the present work we generalize this approach and implement (10) in a non-local sense as

$$(\bar{\boldsymbol{\sigma}}(\mathbf{x}) - \bar{\lambda}_i \mathbf{I})\bar{\mathbf{v}}_i = \mathbf{0}, \quad \text{no summation over } i, \tag{11}$$

where we have introduced the definition for an average element stress $\bar{\boldsymbol{\sigma}}$ according to

$$\bar{\boldsymbol{\sigma}} = \frac{1}{\sum_{R_i < R_{\text{char}}} v_i} \sum_{R_i < R_{\text{char}}} \boldsymbol{\sigma}_i v_i, \quad \text{no summation over } i, \tag{12}$$

computed over all elements with their center in a sphere with the characteristic radius $R_{\text{char}}$. Consequently, $\bar{\lambda}_i$ and $\bar{\mathbf{v}}_i$ denote the eigenvalues and eigenvectors, respectively, and we define here the eigenvector $\mathbf{n} = \bar{\mathbf{v}}_1$ as the one related to the largest eigenvalue of the eigenvalue problem (11). The quantities $\boldsymbol{\sigma}_i$ and $v_i$ characterize the Cauchy stress tensor and the spatial volume related to the $i$th finite element, respectively. The length $R_i = |\mathbf{X}^{\text{c}} - \mathbf{X}_i^{\text{c}}|$ denotes the distance between the referential position $\mathbf{X}_i^{\text{c}}$ at the center of the $i$th finite element and the referential position $\mathbf{X}^{\text{c}}$ at the center of the finite element under consideration. The user-specified parameter $R_{\text{char}}$ is merely an adjustable numerical parameter chosen through numerical experiments. The parameter $R_{\text{char}}$, which depends on factors such as element size etc., should, however, be chosen as small as possible but large enough to avoid the scatter of the normal vector field. Based on our experience, $R_{\text{char}}$ should be within the range of 2–4 times a characteristic element size to achieve reliable numerical results. Note that only the failure criterion is utilized in a non-local sense but not the formulation of the softening due to damage growth. However, [46] showed that the application of non-local failure criterion can lead to non-physical crack initialization, in particular, at stress (strain) singularities.

A further important detail on utilizing the failure criterion in a numerical way, which is worth to be noted, is the fact that the failure criterion is no longer unique when two (or all three) eigenvalues of (11) have (about) the same value. For example, this can be even observed for the (classical) four point shear test, where about in the middle of the height of the bar the crack propagation may branch off about 90°, which is not the crack path experimentally observed. In order to avoid that, the current implementation uses the inner product of the normal vector $\mathbf{n}$ of the discontinuity to be embedded and the vector $\mathbf{n}_{\text{ave}}$, which is the average of all normal vectors of the already existing crack surface within the sphere with the characteristic radius $R_{\text{char}}$. If the inner product $\mathbf{n} \cdot \mathbf{n}_{\text{ave}}$ is smaller than a certain value (in our case this value was chosen to be 0.5), the algorithm embeds a discontinuity in the finite element of interest equal to the normal vector $\mathbf{n}_{\text{ave}}$.

## 4. Classification of algorithms for tracking the crack path

Different numerical techniques for tracking the crack path were proposed and documented in the literature. In order to summarize these techniques a brief (non-comprehensive) review is provided in this section, characterizing their advantages and disadvantages. In particular, techniques, which capture the representation of non-planar and multiple cracks in 3D are considered. Moreover, algorithms for tracking the crack path, which are suitable to be coupled with finite element

techniques representing embedded discontinuities—for example, based on the mixed enhanced assumed strain method or the partition of unity finite element method (extended finite element method)—are favored.

### 4.1. Level set method

The level set method (LSM) is a numerical scheme developed by Osher and Sethina [38]. It aims at modeling the motion of interfaces, and was recently adopted to model 2D [50] and 3D [26] cracks and their propagations. The LSM uses signed distance functions to describe cracks; for the characterization of one crack one need two signed distance functions, i.e. one defines the crack surface and another one the crack-tip, see Fig. 1.

Given the position of the crack-tip, the two advance vectors, which are computed on the basis of the failure criterion, determine the new position of the crack-tip. The values of the signed distance functions are stored at nodes, and provide the required information for an extended finite element method representation of the strong discontinuity.

One drawback of the LSM is that the level representation requires functions one dimension higher than the dimension of the interface leading to high storage and computational costs. A storage-reduced implementation considers only the levels sets in predefined regions near the crack-tip [50]. Moreover, this technique 'freezes' the already existent crack (as it is physically reasonable), and considers only the incremental growth of the crack. Therefore, the predefined regions needs to be larger than the incremental growth length of the crack. Recently, Ventura et al. [54] stated that the standard LSM, as introduced in [38] with the intention to model moving interfaces, is not ideal for characterizing cracks. They introduced a vector level set method for representing cracks in finite elements. Vector level sets describe a surface in 3D by a four-tuple: the sign of the level set function and the components of the closest point projection to the surface. A significant advantage of the vector LSM compared to the standard LSM is the much simpler algorithmic formulation. The update of the vector level set field involves only a few geometric equations; no partial differential equations need be solved to update the vector level sets [54].

### 4.2. Global tracking

An interesting technique for tracking 2D and 3D cracks is provided in [34,35]. The basic idea is to define a linear thermal problem to be solved before each time step of the original mechanical problem. In order to face the heat conduction problem, one assumes two vector fields $\mathbf{a}$ and $\mathbf{b}$ with the condition $\mathbf{a}\cdot\mathbf{N}=\mathbf{b}\cdot\mathbf{N}=0$, where $\mathbf{N}$ denotes a vector perpendicular to a possible failure surface. The approach requires the definition of $\mathbf{N}$ within the whole continuum, and hence the failure criterion (9) (or alternatively Eq. (10)) needs to be generalized.

The family of surfaces, enveloping both vector fields $\mathbf{a}$ and $\mathbf{b}$, can be described by a temperature-like function $\Theta(\mathbf{X})$ if

$$\left.\begin{aligned}\mathbf{a}\cdot\operatorname{Grad}\Theta=\operatorname{Grad}\Theta\cdot\mathbf{a}=0,\\ \mathbf{b}\cdot\operatorname{Grad}\Theta=\operatorname{Grad}\Theta\cdot\mathbf{b}=0,\end{aligned}\right\}\quad\text{in }\Omega_0 \tag{13}$$

holds. Conditions (13) can be rephrased as an anisotropic heat conduction problem [35]. Once the standard heat conduction problem is solved, for example, using the FEM, and the nodal values of the temperature field are known, then the discontinuity path inside a finite element can be implemented at a pure element level. Note that all topological difficulties which arise, in particular, for 3D problems are addressed by the heat conduction problem.

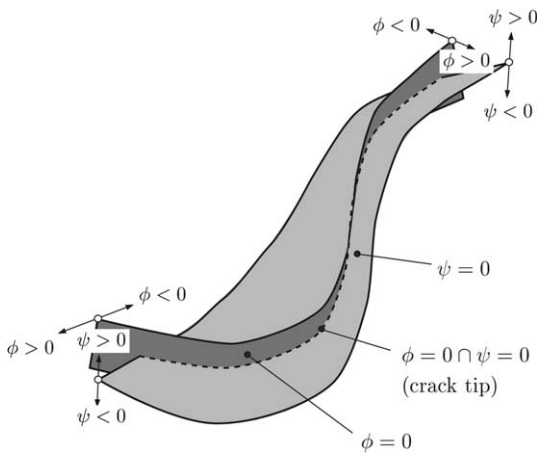


Fig. 1. Level set method: two level sets $\phi$ and $\psi$ defining the crack location, i.e. the crack surface characterized by $\phi\leqslant 0\cap\psi=0$, and the crack-tip characterized by $\phi=0\cap\psi=0$.

Since the algorithm requires the solution of a linear thermal problem before each time step this approach seems to be associated with relatively high computational cost. Moreover, the computation of the normal vector **N** to a possible failure surface for the whole continuum is a drawback of the proposed technique.

### 4.3. Local tracking

A local algorithm is characterized by recursively 'cutting' elements, which has been applied successfully for 2D, see, for example, [55]. To the authors' knowledge the only 3D implementation of this technique is reported in [13]; one reason for that might be arising topological difficulties [35]. We exploited this concept to compute the 3D non-planar crack propagation of multiple non-interacting cracks. For simplicity, in the following section we start with the 2D geometry and then continue to describe this concept for 3D in detail.

## 5. Local algorithm for tracking the crack path

A critical task for applying the concept of PUFEM is the geometrical representation of the crack surface, in particular, in the 3D space. The goal of the proposed algorithm is a geometrical description of multiple non-planar and non-interacting cracks for 3D, which, as a special case, can also be used in 2D.

Throughout this paper it is assumed that the discontinuity within a particular finite element is represented by a flat surface in the reference configuration. Hence, we consider a line embedded in (2D) triangular finite elements, and triangles or (flat) quadrilaterals embedded in (3D) tetrahedral finite elements. Based on this assumption it is trivial to enforce crack path continuity in 2D, while it is, in general, impossible for the 3D case. The topology of a crack in 3D can only be approximated in terms of a non-smooth assembling of triangles and flat quadrilaterals, and continuity can only be enforced along particular lines on the crack surface but not everywhere. Hence, the area of the crack surface is approximated by the proposed scheme leading to an approximation of the fracture dissipation, which depends on the particular application. The authors' experience with the proposed 3D crack surface representation showed that the 'smoothness' of the stress field mainly determines the approximation properties of the crack surface, which itself depends on the mesh size.

### 5.1. Representation of the crack surface in 2D

Basically, the proposed algorithm requires information about: (i) the *potential failure elements*, i.e. those finite elements which have met the failure initialization criterion (for example, the maximum principal stress exceeds the cohesive strength), and (ii) the current *crack-tip data*. For the 2D case this is shown in Fig. 2, where on the left hand side the accumulation of potential failure elements is represented, while on the right hand side crack-tip data in terms of the current tip-point $\mathbf{P}_t$ and tip-facet are sketched. Note that the tip-point $\mathbf{P}_t$ and the tip-facet relate the crack-tip to the location in space and within the finite element mesh, respectively.

A meaningful tracking algorithm for the crack propagation is based on the sequential strung together of line elements as long as the finite element adjacent to the tip-facet is a potential failure element. Hence, the crack propagates until it reaches a finite element, which does not meet the failure initialization criterion. Thereby, the current tip-point and the normal **N** to the discontinuity is utilized. As pointed out in [35] this approach is geometrically spoken nothing more than a *Runge–Kutta*-like algorithm. Hence, the accuracy depends strongly on the geometrical dimension of the region defined by the potential failure elements and basically that means, the larger the load step of the computation the larger the error in tracking the crack surface. Similar techniques are applied in the literature and it is not the scope of this paper to review them.

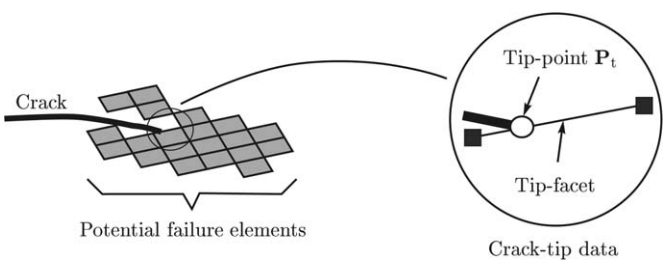


Fig. 2. Representation of the crack surface in 2D: *potential failure elements* are finite elements where the failure initialization criterion is met; *crack-tip data* are given by the current tip-point $\mathbf{P}_t$ and the tip-facet.

### 5.2. Representation of the crack surface in 3D

While the aforementioned concept for 2D can be (more or less) directly implemented, further modifications are required when exploiting the concept in 3D.

In order to proceed we assume a solution of the boundary-value problem at time $t_n$ and the crack-tip data to be known. Furthermore, a number of potential failure elements are accumulated at the crack-tip, and hence the crack will propagate. Without loss of generality, the crack propagation can be considered as a sequence of embedding a discontinuity in the potential failure element located at the front of the current crack. Hence, it is sufficient to discuss the embedding of a discontinuity in a single finite element.

As noted above we assume that the proposed PUFEM uses referential discontinuities that are flat (triangles or quadrilaterals) within a particular finite element. Hence, the referential geometry, i.e. orientation and location of a particular flat discontinuity in the reference configuration of a finite element, is uniquely defined by its normal vector $\mathbf{N}$ and a single point $\mathbf{P}$ located at the discontinuity. While the underlying stress field (e.g., the direction of the maximum principal stress), characterizes the orientation $\mathbf{N}$, the point $\mathbf{P}$ is determined by the adjacent crack front.

For clarification we characterize the crack-tip data by means of triangular tip-facets and tip-points $\mathbf{P}_t$, as shown in Fig. 3(a). By assuming that the finite element through which the crack should propagate shares, in general, $n \in \{1,2,3,4\}$ facets with the crack-tip, we use the definition $\mathbf{P} = \sum_{i=1}^{n} \mathbf{P}_{t\,i}/n$ of the point $\mathbf{P}$ on the discontinuity. For a sketch of this geometrical situation see Fig. 3(b), in which the finite element shares two facets ($n = 2$) with the crack-tip.

So far the described technique may be seen as a generalization of the 2D crack tracking algorithm to 3D. As mentioned above, a successful implementation of this technique for 3D requires some modifications:

(i) A potential source of problems is caused by the non-smooth crack surface, namely, it is not uniquely defined if a particular finite element node belongs to $\Omega_{0+}$ or $\Omega_{0-}$. In order to circumvent this lack of uniqueness, the relevancy of a node is defined once the first related discontinuity is activated.

(ii) The single-step algorithm for predicting the discontinuity, subsequently called the *predictor step*, is a very simple one, and it has given satisfying results for several applications [13]. For the applications presented in this paper, however, the (basis) algorithm was not able to provide satisfying results, and hence a post-processing *corrector step*, which smoothes out the surface, was developed. Details of the proposed two-step scheme are presented in the following section.

#### 5.2.1. Representation of the crack surface in 3D with a smoothing algorithm

For the above introduced predictor step it was assumed that the point $\mathbf{P}$ on, and the orientation $\mathbf{N}$ of a discontinuity are determined by the adjacent crack front and the stress field, respectively. For some situations the prediction obtained by this approach does not fit (very) well to the already existing crack surface and for some circumstances it is not possible to 'close' an existing crack, as schematically shown in Fig. 4. The thick solid line in Fig. 4(a) indicates the crack front of a possible crack, which is represented by the non-smooth assemblage of triangles and (flat) quadrilaterals. The dashed triangle (characterized by $\mathbf{P}$ and $\mathbf{N}$) in Fig. 4(b) shows the predicted discontinuity according to the predictor step, which does not fit (very) well to the existing crack. A corrector step, based on a smoothing strategy (to be discussed subsequently), can avoid these problems and gives a much more appropriate prediction of the discontinuity (characterized by $\mathbf{P}$ and $\mathbf{N}^{\star}$), as it is schematically illustrated in Fig. 4(c). These sketches attempt to assert that the predictor step may not be able to close

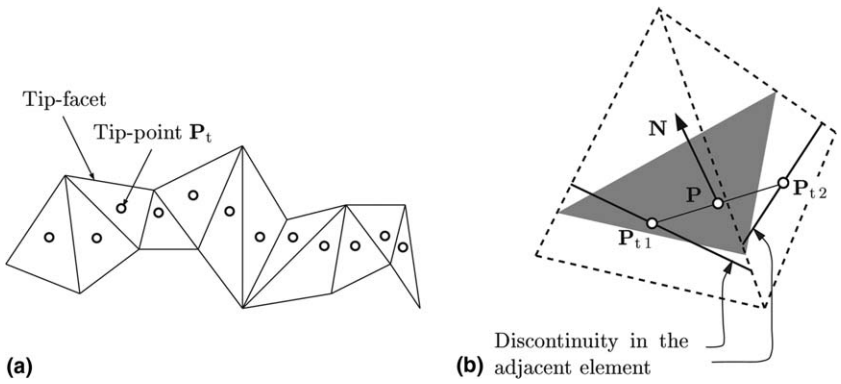


Fig. 3. Definition of the crack surface in 3D: (a) Characterization of the crack-tip by means of tip-facets and tip-points. (b) Propagation of the crack through a particular finite element, which shares two facets with the crack-tip.

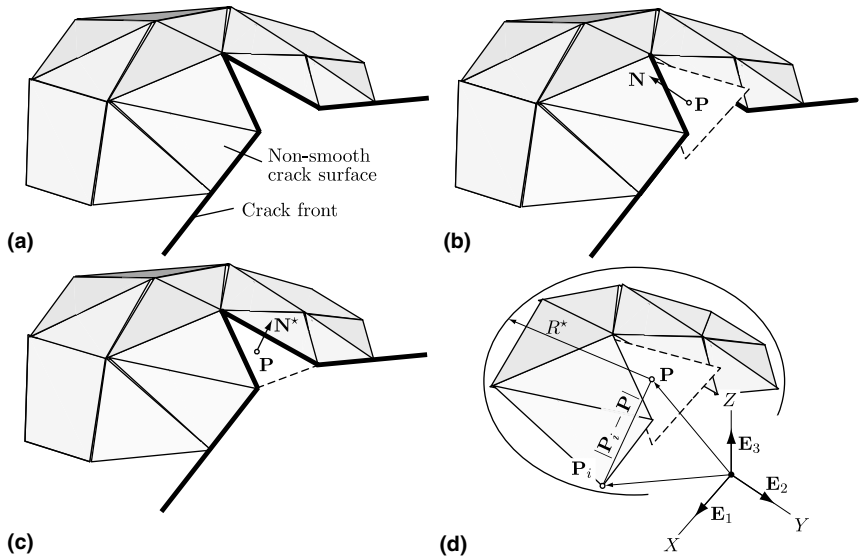


Fig. 4. Sketch showing the prediction of a discontinuity (indicated by the dashed triangles) to be considered for a particular finite element: (a) existing crack characterized by the non-smooth crack surface and the crack front; (b) discontinuity, characterized by **P** and **N**, as predicted by the basic algorithm, which may not be able to 'close' the crack surface; (c) discontinuity, characterized by **P** and $\mathbf{N}^\star$, as predicted by the proposed smoothing algorithm; (d) identification of all discontinuities within a sphere of radius $R^\star$ by means of the condition $|\mathbf{P}_i - \mathbf{P}| < R^\star$.

the existing crack surface; it rather leads to a 'bumpy' crack surface, which may lead to (unphysical) crack bifurcations to be avoided. This is due to the circumstance that the orientation **N** considers too little geometrical information with respect to the crack in the neighborhood of the discontinuity. In order to change the orientation of the discontinuity of interest (from **N** to $\mathbf{N}^\star$) we fit a surface to the crack in the neighborhood of the discontinuity of interest, and use this surface for the definition of the (corrected) orientation $\mathbf{N}^\star$. By doing so the crack surface gets 'smoother', i.e. the discontinuity of interest fits (much) better to the existing crack surface. Note, however, that this approach violates, in general, the (local) failure criterion introduced above, but overcomes several difficulties associated with tracking the crack path in 3D.

In order to explain the corrector step in more detail, we assume that the already existing (non-smooth) crack surface, which includes the discontinuity given by the predictor step, is represented by $n$ nodes. The nodes are the corners of the involved triangles and (flat) quadrilaterals. They are characterized by the position vectors $\mathbf{P}_i$, $i = 1, \ldots, n$, relative to a fixed (global) Cartesian coordinate system $(X, Y, Z)$, which is defined by the set $\{\mathbf{E}_1, \mathbf{E}_2, \mathbf{E}_3\}$ of orthonormal basis vectors. In addition, we introduce a sphere of radius $R^\star$ centered at **P**, and consider the nodes $\mathbf{P}_i$ inside the sphere, which satisfy the condition

$$|\mathbf{P}_i - \mathbf{P}| < R^\star, \quad i = 1, \ldots, n. \tag{14}$$

For the geometrical illustration see Fig. 4(d). Hence, we get the total number of nodes of the triangles and (flat) quadrilaterals within the sphere, $n_{R^\star}$ say, where it is worth noting that the nodes of the discontinuity according to the predictor step are included. All these nodes characterized by the position vectors $\mathbf{P}_i$, $i = 1, \ldots, n_{R^\star}$, form a point cloud and are used for the proposed smoothing procedure. Note that $R^\star$ is merely an adjustable (user-specified) numerical parameter.

For a straightforward representation of a surface fitted to the determined point cloud, we compute the centroid (mean) $\mathbf{P}_c = \sum_{i=1}^{n_{R^\star}} \mathbf{P}_i / n_{R^\star}$ of the point cloud and place a (local) Cartesian coordinate system $(\overline{X}, \overline{Y}, \overline{Z})$ there, see Fig. 5. It is characterized by a fixed set $\{\mathbf{e}_1, \mathbf{e}_2, \mathbf{e}_3\}$ of orthonormal basis vectors, which are defined by a principal component (axes) analysis of the point cloud. Consequently, we introduce the covariance tensor $\mathbf{D} = \sum_{i=1}^{n_{R^\star}} (\mathbf{P}_i - \mathbf{P}_c) \otimes (\mathbf{P}_i - \mathbf{P}_c)$ of the point cloud, and the set $\{\mathbf{e}_1, \mathbf{e}_2, \mathbf{e}_3\}$ of basis vectors is then defined by the eigenvalue problem of **D**, i.e. $(\mathbf{D} - \lambda_i \mathbf{I})\mathbf{e}_i = \mathbf{0}$, $i = 1, 2, 3$ (no summation over $i$). Hence, we find the eigenvalues $\lambda_1$, $\lambda_2$, $\lambda_3$ and the associated eigenvectors, which are the basis vectors $\mathbf{e}_1$, $\mathbf{e}_2$, $\mathbf{e}_3$ defining the corresponding principal axes and characterizing the 'orientation' of the point cloud. We assume that the eigenvectors are sorted such that they relate to the eigenvalues $\lambda_1 > \lambda_2 > \lambda_3$, for example, $\mathbf{e}_3$ is related to the smallest eigenvalue $\lambda_3$.

Within the Cartesian coordinate system $(\overline{X}, \overline{Y}, \overline{Z})$ at $\mathbf{P}_c$, given by the basis vectors $\mathbf{e}_1$,$\mathbf{e}_2$,$\mathbf{e}_3$, either a surface described by the linear function $\overline{Z} = a_0 + a_1\overline{X} + a_2\overline{Y}$, or by the quadratic function $\overline{Z} = a_0 + a_1\overline{X} + a_2\overline{Y} + a_3\overline{X}^2 + a_4\overline{Y}^2 + a_5\overline{X}\overline{Y}$ is then fitted to the $n_{R^\star}$ nodes of the point cloud. Hence, the set $(a_0, \ldots, a_2)$ or $(a_0, \ldots, a_5)$ of coefficients are defined by minimizing the least-square problem

$$\Phi = \sum_{i=1}^{n_{R^\star}} (\overline{Z}_i - \overline{Z}(\overline{X}_i, \overline{Y}_i))^2 \to \mathrm{MIN}, \tag{15}$$

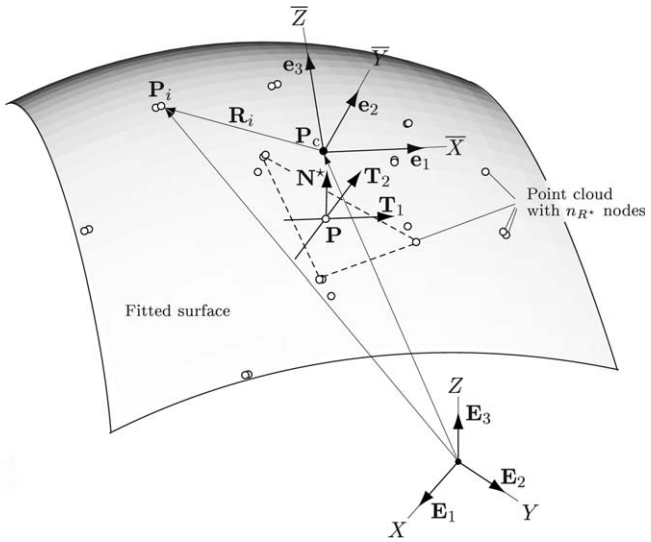


Fig. 5. Geometrical situation of a surface fitted to a point cloud with $n_{R^\star}$ nodes: centroid of the point cloud $\mathbf{P}_c$ placed in a (local) coordinate system $(\overline{X},\overline{Y},\overline{Z})$; position vector $\mathbf{P}_i$ of a typical node $i$ with distance $\mathbf{R}_i = \mathbf{P}_i - \mathbf{P}_c$ from $\mathbf{P}_c$ relative to a (global) coordinate system $X$, $Y$, $Z$; improved normal vector $\mathbf{N}^\star = \mathbf{T}_1 \times \mathbf{T}_2$ at $\mathbf{P}$ with tangent vectors $\mathbf{T}_1 = \partial\overline{Z}/\partial\mathbf{e}_1$ and $\mathbf{T}_2 = \partial\overline{Z}/\partial\mathbf{e}_2$.

where $X_i$, $Y_i$, $Z_i$ denote the components of the position vector $\mathbf{P}_i$ of a typical node $i$ relative to the fixed origin. Eq. (15) leads to the solution of a symmetric and linear system of equations for the coefficients involved, see Appendix A. Note that the evaluation of (15) is performed within the local coordinate system, and hence the components of the position vectors $\mathbf{P}_i$ are associated with the (local) orthonormal system $\mathbf{e}_1$, $\mathbf{e}_2$, $\mathbf{e}_3$. The relation between the components of the *loc*al and the *glo*bal frames for the vectors $\mathbf{P}_i$ are given by $[\mathbf{P}_i]_{\text{loc}} = [\mathbf{Q}]^{\text{T}}[\mathbf{P}_i]_{\text{glo}} - [\mathbf{P}_c]_{\text{glo}}$, where $[\mathbf{Q}]$ is the matrix representation of a proper orthogonal tensor $\mathbf{Q}$ ($\det\mathbf{Q} = +1$). The orthogonal matrix $[\mathbf{Q}]$ contains the collection of the components $Q_{ij}$. By assuming the specific components $[\mathbf{E}_1] = [1,0,0]^{\text{T}}$, $[\mathbf{E}_2] = [0,1,0]^{\text{T}}$, $[\mathbf{E}_3] = [0,0,1]^{\text{T}}$ of the global basis vectors, the components $Q_{ij} = \mathbf{E}_i \cdot \mathbf{e}_j$ are simply given by $Q_{ij} = e_{ij}$, where $e_{ij}$ denotes the $i$th component of the $j$th basis vector $\mathbf{e}_j$.

Once the coefficients, i.e. $(a_0,\ldots,a_2)$ or $(a_0,\ldots,a_5)$ are defined, the components of the improved normal vector $\mathbf{N}^\star$ at $\mathbf{P}$ reads $\mathbf{N}^\star = \mathbf{T}_1 \times \mathbf{T}_2$, with the tangent vectors $\mathbf{T}_1 = \partial\overline{Z}/\partial\mathbf{e}_1$ and $\mathbf{T}_2 = \partial\overline{Z}/\partial\mathbf{e}_2$ (see Fig. 5). With respect to the local frame the components of the tangent vectors read $[\mathbf{T}_1] = [1,0,a_1 + 2a_3\overline{X} + a_5\overline{Y}]$ and $[\mathbf{T}_2] = [0,1,a_2 + 2a_4\overline{Y} + a_5\overline{X}]$, where $a_3 = a_4 = a_5 = 0$ for the case that the surface to be interpolated is a linear function. Finally, the components of the improved normal vector $\mathbf{N}^\star$ are required with respect to the global frame, and are determined according to $[\mathbf{N}^\star]_{\text{glo}} = [\mathbf{Q}][\mathbf{N}^\star]_{\text{loc}}$.

A summary of the involved tasks defining the corrector step is provided in Table 1. Note that the corrector step can only be applied if a crack already exists, and hence at the beginning of a crack propagation we have to use the predictor step solely. From a practical point of view, this causes no problems since at that stage the stress field (which mainly determines the propagation of a crack surface) at the crack-tip is usually observed to be smooth.

### 5.2.2. Implementation of the two-step algorithm for tracking the 3D crack path

The implementation of the algorithm for tracking the 3D crack path is based on an user-defined macro, running within the multi-purpose finite element software FEAP [51]. Therefore, the introduced common blocks `CTIP` and `CTET` store the data associated with the crack-tip (tip-point and tip-facet), and the potential failure elements, $n_f$ say, respectively. In particular, the potential failure elements are defined in a separate numerical routine, which has access to all state variables of all finite elements. Therefore, it is straightforward to implement any failure criterion. In addition, we introduced the common block `NOID` which stores the relevancy of the finite element nodes (belonging either to $\Omega_{0+}$ or to $\Omega_{0-}$), subsequently

Table 1
Summary of the corrector step based on a smoothing strategy of the crack surface

- Define the $n_{R^\star}$ points $\mathbf{P}_i$ of the point cloud according to $|\mathbf{P}_i - \mathbf{P}| < R^\star$, $i = 1,\ldots,n$
- Compute the centroid $\mathbf{P}_c$ and the covariance tensor $\mathbf{D}$ of the point cloud $\mathbf{P}_c = \sum_{i=1}^{n_{R^\star}} \mathbf{P}_i/n_{R^\star}$, $\mathbf{D} = \sum_{i=1}^{n_{R^\star}} (\mathbf{P}_i - \mathbf{P}_c) \otimes (\mathbf{P}_i - \mathbf{P}_c)$
- Define the set $\{\mathbf{e}_1,\mathbf{e}_2,\mathbf{e}_3\}$ of the local basis vectors by solving $(\mathbf{D} - \lambda_i\mathbf{I})\mathbf{e}_i = \mathbf{0}$, $i = 1,2,3$ (no summation over $i$)
- Define the set $(a_0,\ldots,a_2)$ or $(a_0,\ldots,a_5)$ of coefficients by solving $\Phi = \sum_{i=1}^{n_{R^\star}} (\overline{Z}_i - \overline{Z}(\overline{X}_i,\overline{Y}_i))^2 \rightarrow \text{MIN}$
- Compute corrected orientation of the discontinuity $\mathbf{N}^\star = \mathbf{T}_1 \times \mathbf{T}_2$ with $\mathbf{T}_1 = \partial\overline{Z}/\partial\mathbf{e}_1, \mathbf{T}_2 = \partial\overline{Z}/\partial\mathbf{e}_2$

called 'enhancement information'. In order to serve the PUFEM formulation with the required data on the element level, for example, the geometry and shape (triangle or quadrilateral) of the discontinuity, FEAPs blank-common block is used.

Moreover, we have to define *crack roots*, i.e. potential crack initializations in the associated finite elements. The crack roots are characterized by means of (root) tip-points, which define the location where the cracks are allowed to start. At the present implementation the user has to define the crack roots (which are located at the notches for the numerical examples represented in the next section), however, an automatic definition of crack roots would be desirable. Here it needs to be emphasized, that large load steps can cause complicated agglomerations of potential failure elements, and hence an automatic definition of crack roots might get quite difficult.

Once the crack root is defined and stored in `CTIP`, the propagation of the crack can be evaluated. For a flow chart of the required sequences processed by the crack-propagation package see Fig. 6. Primarily, the algorithm is determined by two nested loops, where the inner loop runs over all $n_f$ potential failure elements, which are stored in `CTET`. The outer loop is repeated until the truncation flag *cut* is `TRUE`, therein, a specific potential failure element is denoted by $i$. Whenever a potential failure element is located on the crack-tip, in the sense that one or more tip-facets coincide with one or more element facets, a sequence of tasks for the $i$th potential failure element is executed.

(i) The *predictor step* computes a (trial) discontinuity based on **P** and **N**. As discussed in Section 5.2, **P** and **N** are determined by the adjacent crack front and the stress field, respectively.
(ii) The *corrector step* modifies (corrects) the orientation of the discontinuity by the proposed smoothing algorithm discussed in Section 5.2.1 (see Table 1), and consequently, an improved discontinuity is introduced in the finite element.
(iii) Once the discontinuity is introduced in the $i$th finite element, the algorithm computes and stores all relevant data for the PUFEM formulation, e.g., the shape (triangle or quadrilateral) of the discontinuity, the enhancement information, etc. In addition, the crack-front is advanced through the $i$th finite element by computing new tip-data (crack-facets and tip-points), which are stored in `CTIP`. Finally, the $i$th finite element gets inactive with respect to the crack-propagation algorithm.

Once the loop over all potential failure elements is executed, `CTET` is updated by removing those elements, which were inactivated during the previous task, and the potential failure elements $n_f$ are re-defined. Finally, the enhancement information in `NOID` is modified such that the crack is enforced to be closed at the crack-tip, i.e. all finite element nodes forming the crack-tip are not allowed to be enhanced. Note that this constraint is physically motivated and crucial for the stability of the finite element computation of the problems discussed in Section 6.

#### 5.2.3. Identified problem and possible remedy

The proposed algorithm assumes that each discontinuity in the reference configuration is fixed once it is embedded. Hence the algorithm is not able to change already existing cracks, which represent physical discontinuities. However, the proposed approximation of the crack surface might require a re-definition of the discontinuities at the crack-tip, which is illustrated in Fig. 7.

For simplicity, and without loss of generality, the problem is illustrated for the 2D case. Fig. 7(a) shows a possible geometrical situation at a crack-tip. The quantities $\mathbf{P}_{to}$ and $\mathbf{N}_o$ characterize the tip-point and the normal to the discontinuity (crack), respectively. The subscript $(\bullet)_o$ denotes quantities of an old (previous) state. As can be seen from Fig. 7(a) the angle between the tip-facet and the discontinuity is (very) small, and in the particular case, the algorithm drives the crack into the opposite direction, as illustrated in Fig. 7(b). Here, $\mathbf{P}_{tn}$ and $\mathbf{N}_n$ denote the tip-point and the normal to the discontinuity predicted by the algorithm, where the subscript $(\bullet)_n$ indicates quantities obtained from the new (current) solution. While this type of crack propagation is pathological and terminates, in general, a 2D computation, it leads to local stress concentrations (temporarily) and 'holes' (permanently) in the crack surface in 3D. Since it turns out that the situation illustrated in Fig. 7(a), which may lead to a crack propagation as pointed out in Fig. 7(b), happens rarely during an actual 3D computation, the consequences of this phenomenon on the global results are negligible in practice (at least in 3D). However, the authors observed that the related local stress concentrations might cause (non-physical) secondary cracks, which, when joining the primary crack, can also terminate the 3D computation. In order to avoid crack propagations according to Fig. 7(b) we would have to re-define the (existing) discontinuities at the crack-tip according to the re-defined normal $\mathbf{N}_o^{new}$ of the old (previous) state, as illustrated in Fig. 7(c), where the dashed line indicates the re-defined discontinuity. Since the required re-definition of the discontinuity of the old (previous) state is not possible with the algorithm proposed (see Fig. 6), we apply a simple but effective solution of this problem. Namely, we locally constrain the normal vector to be perpendicular to the adjacent edge (in 2D) or facet (in 3D) of the finite element, see Fig. 7(d).

It is worth noting that, strictly spoken, the prediction by the proposed remedy depends on the underlying finite element mesh, although, practically, the associated mesh-dependency is negligible. This is probably due to the fact that the generated error, i.e. the difference between the predictions shown in Fig. 7(c) and (d), depends (strongly) on the angle between $\mathbf{N}_n$ and $\mathbf{N}_o$, which is, in general, very small for the discussed situation. Moreover, practically only a few crack facets are

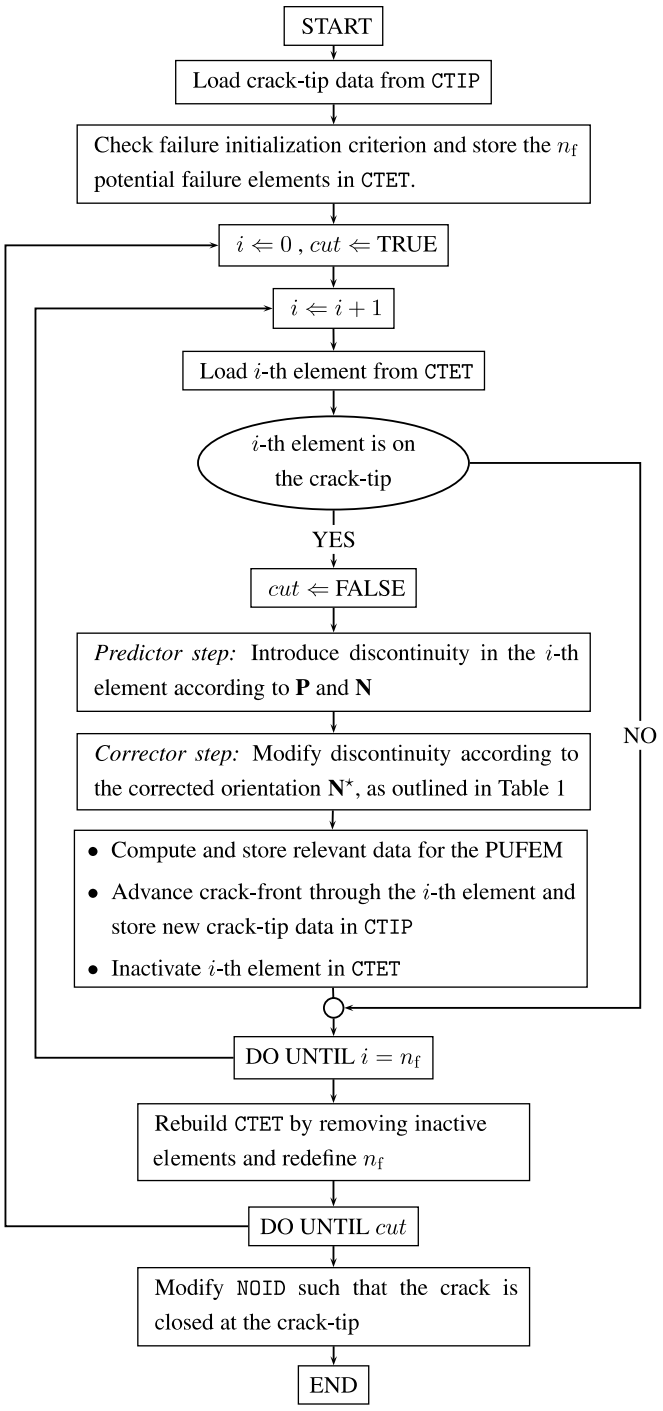


Fig. 6. Flow chart of the required sequences processed by the crack-propagation package.

affected by the proposed remedy, for example, for the *Brokenshire test*, as analyzed in Section 6.2, about 140 of about 2800 crack facets were treated by the proposed remedy, i.e. 5.0%.

*5.2.4. Consequences of the proposed smoothing algorithm*

The basic motivation of the proposed smoothing algorithm is to avoid difficulties arising from a geometrically incompatible prediction of the crack surface according to the applied failure criterion. The proposed non-local definition of the crack surface naturally effects the propagation of multiple cracks close to each other. Here, 'close to each other' is defined by the radius $R^\star$, and the effect of the smoothing strategy depends on the problem. For example, let us consider a simple direct tension test, where two cracks approach each other. Without a smoothing strategy the two cracks would, in general, not meet each other. However, the application of the proposed smoothing step enforces the two crack fronts to find each

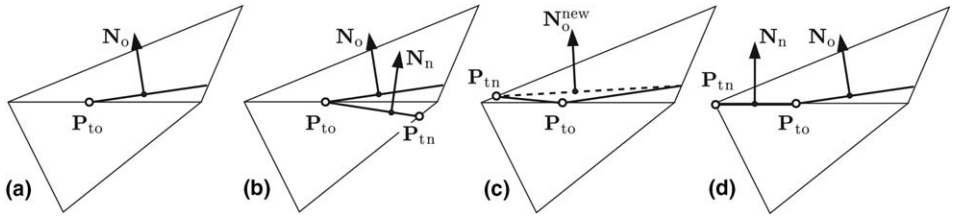


Fig. 7. Discontinuity at a crack-tip illustrated for the 2D case: (a) possible geometrical situation at a crack-tip characterized by $\mathbf{P}_{to}$ (tip-point) and $\mathbf{N}_o$ (normal to the discontinuity) of an old (previous) state; (b) prediction of the local crack tracking algorithm causes crack growth into the opposite direction—the crack-tip is characterized by $\mathbf{P}_{tn}$ and $\mathbf{N}_n$ obtained from a new (current) state; (c) modification with re-definition of the existing discontinuity—not possible with the algorithm (the dashed line indicates the re-defined discontinuity according to the re-defined normal $\mathbf{N}_o^{new}$ of the old (previous) state); (d) modification without re-definition of the existing discontinuity, i.e. $\mathbf{N}_n$ is perpendicular to the adjacent finite element edge.

other (assuming the crack fronts are not too far away from each other), and hence a closed crack surface may develop, which also reflects the physical solution. For the more general situations, and, in particular, where the approaching cracks have significant different normals, the proposed smoothing strategy fails most likely. However, it needs to be emphasized, that the evolution of multiple and non-interacting crack can be handled by the introduced concept once each crack is treated separately. This guarantees that the evolution of a particular crack is not effected by the geometry of the others.

## 6. Representative numerical examples

The introduced computational framework, i.e. the partition of unity finite element method combined with the proposed tracking algorithm for non-planar 3D cracks, has been employed for the prediction of concrete failure; two representative numerical examples are analyzed in detail and compared with experimental and numerical data known from the literature. In particular, the two examples embrace the *Nooru-Mohamed test*, a mixed mode fracture test undertaken at Delft University of Technology in (1992) [29], and the *Brokenshire test*, a torsion fracture test undertaken at Cardiff University in (1996) [9]. These examples aim at modeling the quasi-brittle failure of unreinforced concrete, where no compressive crushing and aggregate interlocking is assumed to be present. Hence, we assume that in the localization zone the cohesive properties of the material dominate over the frictional properties, and the corresponding failure mode exhibits fracture in the form of separation bands rather than friction along shear bands (see [41]). The presented computations are performed on a PENTIUM 4 PC with 1.0 GB RAM. The unstructured finite element meshes are generated with the software-package NETGEN [43] and the mesh is a priori refined in those regions were failure was expected.

### 6.1. Simulation of the Nooru-Mohamed test

The Nooru-Mohamed test applies tensile and shear loads to a double-edge-notched specimen (DENS), for which a number of loading paths were experimental investigated [29]. It is well known that this test can be considered as a 2D problem, which is also confirmed by our computation. However, the aim of the present study is to investigate the proposed algorithm for tracking the crack path with respect to multiple (two) non-interacting and non-planar cracks. The dimensions of the DENS and the considered loading and boundary conditions are illustrated in Fig. 8. In particular, we investigate the loading protocol 4b, as defined in [29]. For that specific protocol the loading path for the DENS is comprised by two steps: (i) applying a shear load $P_s$ of 10.0 kN while keeping the normal load $P_n$ at zero, and (ii) applying a normal load $P_n$, while keeping the shear load $P_s$ fixed at 10.0 kN. In the following the numerical findings are labeled with the opening displacement $\delta$, which is defined as the relative displacement between the points $A$ and $B$ (or alternatively between $A'$ and $B'$) in the direction of the normal load $P_n$, as illustrated in Fig. 8.

Because of the specific loading protocol the principal stresses rotate during the test, resulting in two curvilinear cracks. The *Nooru-Mohamed test* has been numerically investigated by several authors using different numerical and constitutive approaches, see, for example, [22,39,40] among others. For the present computation, we used material parameters as shown in Table 2, and applied a finite element discretization using 32311 constant strain tetrahedral elements. Note that the parameters $t_0$, $a$, $b$, $\alpha$ of the cohesive zone lead to a mode I fracture energy of $\mathscr{G}_f^I = 0.106\ \mathrm{N\ mm^{-1}}$ [13]. Hence the quantified constitutive response of the *Nooru-Mohamed test* can be compared to that used in [40]. In order to define the failure criterion of the $i$th finite element according to Eq. (12), the Cauchy stress is averaged within the sphere of radius $R_{\mathrm{char}} = 3.0\sqrt[3]{v_i}$, where $v_i$ denotes the current element volume. Moreover, the orientation $\mathbf{N}^\star$ of the discontinuity to be embedded in the $i$th finite element is characterized by a corrector step (see Section 5.2.1), which utilizes a quadratic surface for the smoothing algorithm. Thereto, the surface is fitting to the nodes of the (non-smooth) crack surface within a sphere of $R^\star = 4.0\sqrt[3]{V_i}$, where $V_i$ denotes the referential volume of the $i$th finite element.

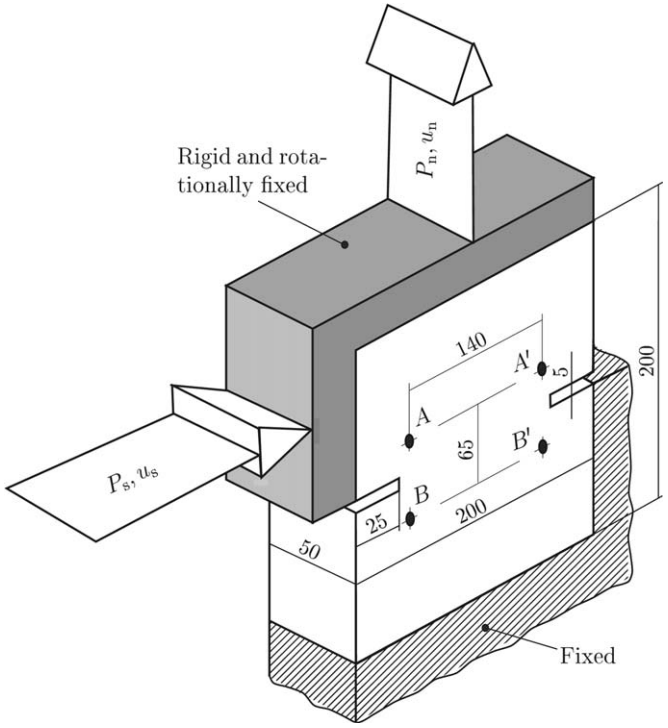


Fig. 8. *Nooru-Mohamed test* [29]: double-edge-notched specimen (DENS) applied to loading and boundary conditions (all dimensions are in millimeter).

Table 2
Bulk and cohesive material parameters applied

| | |
|---|---|
| *Bulk material response* | |
| Bulk modulus, $\kappa$ | $16.67 \times 10^3$ MPa |
| Shear modulus, $\mu$ | $12.50 \times 10^3$ MPa |
| *Cohesive material response* | |
| Cohesive tensile strength, $t_0$ | 3.0 MPa |
| Cohesive parameter, $a$ | 11.32 $\text{mm}^{-1}$ |
| Cohesive parameter, $b$ | 0.674 |
| Anisotropy parameter, $\alpha$ | 1.0 |

Fig. 9 shows the deformed configurations and the related maximum principal Cauchy stress at the opening displacement $\delta = 0.048$ mm, where the displacements are scaled by a factor 500. It illustrates the two evolved cracks and the stress concentrations at the crack-tips. In addition, Fig. 10 shows the evolving discontinuities with respect to the reference configuration at the opening displacements $\delta = 0.006, 0.017, 0.5$ mm. As can be seen, the two 'symmetrical' and curvilinear cracks are developing as expected. Note that we have used a completely unstructured mesh, hence the symmetry of both evolving cracks indicates no mesh sensitivity of the proposed method.

In Fig. 11 the computed crack formation is compared to experimental data [29]. The comparison indicates a good correlation between the numerical prediction and the experimental observation, in particular for the upper crack. In addition, the initiation of the cracks at an angle of about 50° with respect to the normal loading direction is captured very nicely. Note that the experiment does not show the expected symmetry of both cracks.

A comparative study of the evolution of the normal load $P_n$ with respect to the opening displacement $\delta$ is presented in Fig. 12. Experimental data are according to [29] and shown by a grey solid line, while the results of the recent numerical analysis [40] is shown by the dashed line. Our results obtained, with the PUFEM formulation combined with the proposed tracking algorithm for non-planar 3D cracks and using an unstructured mesh are characterized by the solid black line in Fig. 12. Note that the work [40] investigated the *Nooru-Mohamed test* on the basis of the extended Leon model, two multi-surface plasticity formulations and a microplane model. The authors concluded that the microplane model provided the closest results to the experimental data, and these results are also illustrated in Fig. 12. As can be seen, our numerical prediction can be compared with the results predicted by the microplane model executed in [40]. While the present computation seems to capture small opening displacements more accurately it resulted in worse results at larger opening

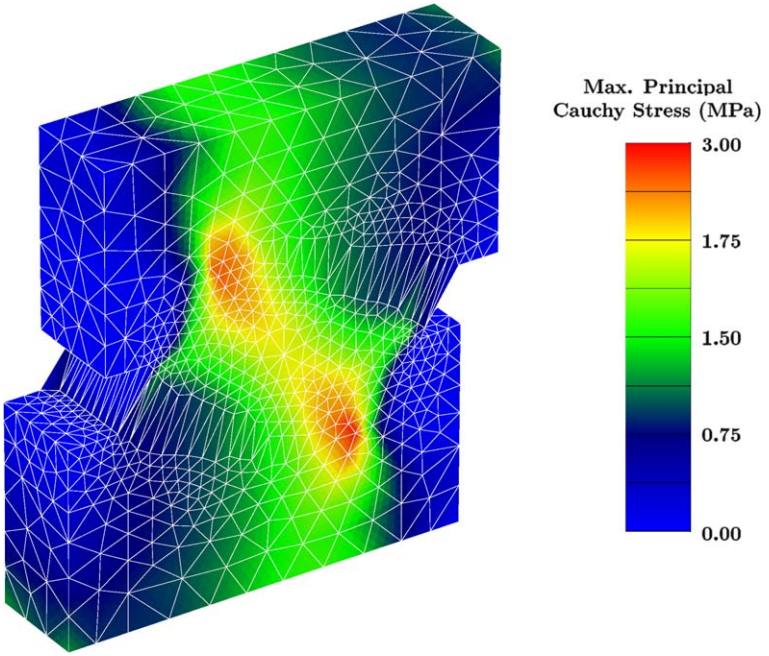


Fig. 9. *Nooru-Mohamed test*: maximum principal Cauchy stress superimposed on the current configuration at the opening displacement $\delta = 0.048$ mm (displacements are scaled by a factor 500).

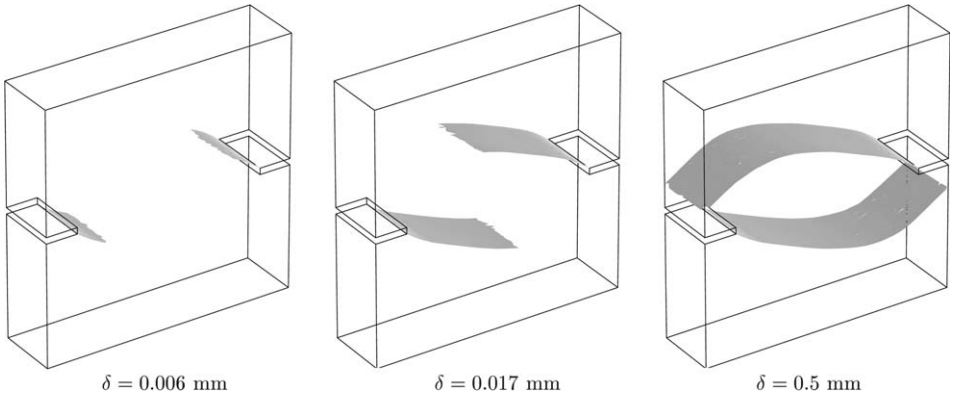


Fig. 10. *Nooru-Mohamed test*: evolution of two 'symmetrical' and curvilinear cracks. Three particular opening displacements are considered, i.e. $\delta = 0.006$, 0.017, 0.5 mm. Illustrated cracks are with respect to the reference configuration.

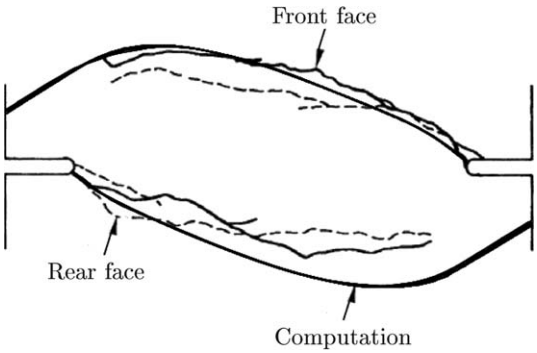


Fig. 11. *Nooru-Mohamed test*: numerically predicted and experimentally observed crack formation of the double-edge-notched specimen (DENS) applied to loading and boundary conditions according to the Nooru-Mohamed test [29], as illustrated in Fig. 8.

displacements when compared to the experimental data. A significant overestimation of the limit load is predicted by both numerical approaches when compared to the experimental data. Finally, note that a similar overestimation of the limit load

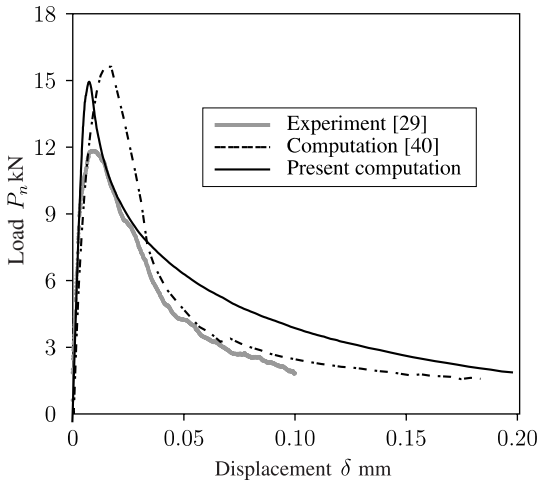


Fig. 12. Normal load–displacement ($P_n$-$\delta$) curves for the *Nooru-Mohamed test*: the grey solid line denotes experimental data published in [29], the dashed line represents numerical results given in [40], and the solid black line denotes our computation, which combines the PUFEM formulation with the proposed tracking algorithm for non-planar 3D cracks using a completely unstructured mesh.

was reported in [22] using Rankine gradient-dependent plasticity model, which was not able to capture the curved character of the evolving cracks.

### 6.2. Simulation of the Brokenshire test

The capability and efficiency of the proposed method, in particular, of the proposed tracking algorithm for capturing non-planar 3D cracks is now studied by means of the torsion fracture test, i.e. the *Brokenshire test*, as documented in [9]. The dimensions of a notched prismatic specimen with the applied loading and boundary conditions are illustrated in Fig. 13. Three supports fix the specimen and a downward oriented force $P$ with related displacement $u$ characterizes the loading of the *Brokenshire test*. The *Brokenshire test* requires a fully three-dimensional formulation. On the basis of a plastic–damage-contact model and a predefined crack path this example has recently been investigated numerically in the work [18]. Based on the particular loading, a non-planar crack starts to propagate at the notch. Subsequently, all results are considered with respect to the crack mouth opening displacement (CMOD), which is defined as the relative displacement between the points $A$ and $B$ normal to the notch, see Fig. 13.

For the present computation we used the same material parameters as before (for a summary see Table 2). The applied finite element discretization uses 40610 constant strain tetrahedral elements; a quasi-static and displacement-controlled computation is performed. Moreover, the failure criterion and the orientation of the discontinuities are characterized by the non-local measures $R_{\text{char}} = 3.0\sqrt[3]{v}$ and $R^{\star} = (3.0 \div 4.0)\sqrt[3]{V}$, with $v$ and $V$ denoting the current and referential finite element volumes, respectively.

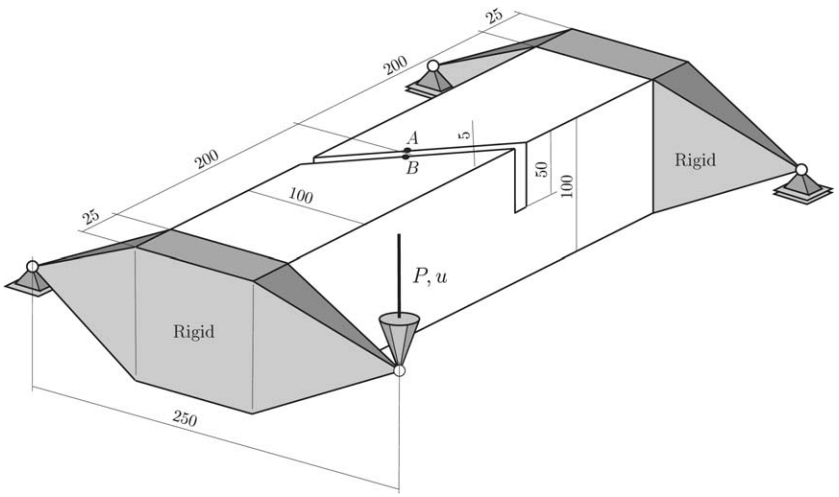


Fig. 13. *Brokenshire test* [9]: notched prismatic specimen applied to loading and boundary conditions (all dimensions are in millimeter).

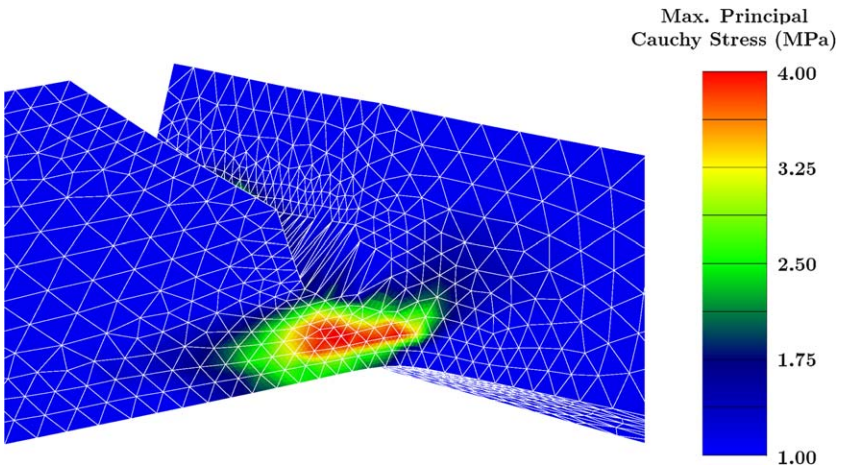


Fig. 14. *Brokenshire test*: maximum principal Cauchy stress superimposed on the current configuration at the maximum load of CMOD = 0.161 mm (displacements are scaled by a factor 500).

Fig. 14 shows the deformed configuration and the related maximum principal Cauchy stress at the crack mouth opening displacement of CMOD = 0.161 mm. For illustrative purposes the displacements are scaled by a factor 500. The figure illustrates the developed crack and the related stress concentration at the crack-tip. In addition, it can be seen that parallel to the crack a region of high principal Cauchy stress is developed, in which inelastic phenomena are probably dominant not captured by the present computation.

Fig. 15 shows the evolving discontinuity with respect to the reference configuration at the crack mouth opening displacements CMOD = 0.044, 0.127, 2.145 mm. As can be seen, a double-curved crack with the expected symmetry develops. Moreover, we investigated the influence of the numerical parameter $R^\star$ on the development of the crack; results are illustrated in Fig. 16. Here two fully developed cracks are compared, which are based on computations with $R^\star = 3.0\sqrt[3]{V}$ and $R^\star = 4.0\sqrt[3]{V}$, respectively. The cracks are investigated at the bottom of the beam, where the largest difference between them is expected. A slight deviation from each other can be observed, but the considered variation of $R^\star$ does not change the

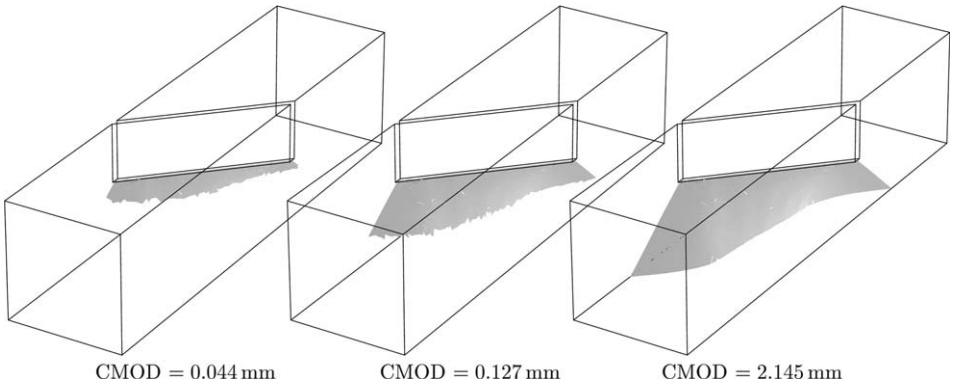


Fig. 15. *Brokenshire test*: evolution of a double-curved crack with respect to the reference configuration at the crack mouth opening displacements CMOD = 0.044, 0.127, 2.145 mm.

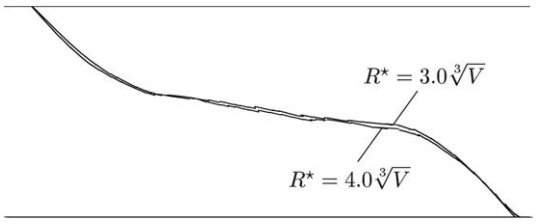


Fig. 16. Influence of $R^\star$ on the evolution of the crack. Predicted cracks at the bottom of the beam for $R^\star = 3.0\sqrt[3]{V}$ and $R^\star = 4.0\sqrt[3]{V}$ are shown, where the largest difference is present.

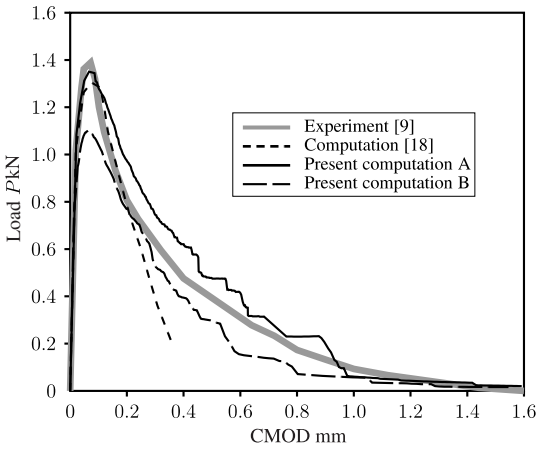


Fig. 17. Load–displacement ($P$-CMOD) curves for the *Brokenshire test*: the grey solid line denotes experimental data published in [9], the (smooth) dashed line represents numerical results given in [18], and the other two lines represent our numerical prediction, which combines the PUFEM formulation with the proposed tracking algorithm for non-planar 3D cracks using a completely unstructured mesh. The solid line ('present computation A') represents numerical results which are based on material parameters summarized in Table 2, while the dashed line ('present computation B') is based on parameters taken from Table 3.

Table 3
Material parameters for the *Brokenshire test* in accordance with [18]

| | |
|---|---|
| *Bulk material response* | |
| Bulk modulus, $\kappa$ | $19.44 \times 10^3$ MPa |
| Shear modulus, $\mu$ | $14.58 \times 10^3$ MPa |
| *Cohesive material response* | |
| Cohesive tensile strength, $t_0$ | 2.3 MPa |
| Cohesive parameter, $a$ | 11.32 $\text{mm}^{-1}$ |
| Cohesive parameter, $b$ | 0.674 |
| Anisotropy parameter, $\alpha$ | 1.0 |

basic crack pattern. However, it needs to be emphasized that for (too) large values of $R^\star$ the crack propagation is mainly determined by the geometry of the already existing crack surface, and the influence of the stress field becomes negligible. Hence, $R^\star$ can be seen as a weighting parameter between the stress field and the geometry which determines the crack propagation.

A comparative study of the evolution of the load $P$ with respect to the crack mouth opening displacement (CMOD) is presented in Fig. 17. Experimental data are taken from [9] and shown by a grey solid line, while our numerical results are indicated by the solid black line in Fig. 17, indicated as 'present computation A'. As can be seen, the present numerical prediction is in good agreement with the experimental data documented in [9]. In particular, the limit load is captured accurately, and the present analysis is able to represent the softening behavior of the material. The scatter of the computed results that exceed CMOD = 0.4 mm is either an inherent (stability) problem or is caused by the relatively coarse unstructured mesh which was used, in particular, at the bottom of the beam.

For comparison purposes numerical results of the recent study [18] are shown by the dashed line in Fig. 17. Moreover, in Fig. 17 we have indicated our numerical results which are based on the material parameters as shown in Table 3 (indicated as 'present computation B'). These parameters are basically proposed in [18]. In particular, the parameters $t_0$, $a$, $b$, $\alpha$ describing the cohesive zone lead to a mode I fracture energy of $\mathscr{G}_{\text{f}}^{I} = 0.082$ N $\text{mm}^{-1}$, hence the quantified constitutive response can be compared to results given in [18]. As can be seen, this set of material parameters leads to a much weaker response of the *Brokenshire test* than that observed by the experiment. In particular, a significant underestimation of the limit load is evident.

## 7. Conclusion

The typical discontinuous pattern, which occurs during failure of unreinforced concrete, were modeled within the framework of strong discontinuities. A cohesive fracture process zone was introduced, and the cohesive material response was described by a transversely isotropic traction separation law, which governs the material-dependent resistance against cracking in a phenomenological sense. A specific cohesive potential was briefly reviewed. The cohesive potential is suitable to describe tensile failure of concrete capturing an exponential decay of the traction with respect to evolving damage (i.e.

separation). Since the well-known necessary condition of strain localization, i.e. the singularity of the acustic tensor, is related to high computational cost when applied to general boundary-value problems to be solved numerically, the simpler Rankine criterion was employed in the present computations leading to sufficiently accurate results. In addition, a non-local smoothing of the stress field was introduced, and hence the failure criterion was implemented in a non-local sense.

After reviewing certain algorithms developed for tracking the crack path, a recently proposed single-step algorithm [13] was described in more detail. The algorithm, denoted as 'predictor step' throughout this paper, is able to drive multiple non-interacting and non-planar cracks in 3D. For simplicity, it was assumed that the discontinuities within the finite elements are flat in the reference configuration, hence, in general, a non-smooth representation of the global crack surface was achieved. In order to overcome topological difficulties, i.e. 'bumpy' crack surfaces which may lead to (unphysical) crack bifurcations, the tracking algorithm was equipped with a corrector step, which draws in non-local information to smooth the surface. The idea is based on a local (first-order or) second-order approximation of the crack surface by considering neighboring discontinuities, and, consequently, by re-defining the normal vector.

The constitutive framework is based on the partition of unity finite element method, which leads to robust and mesh-independent representations of concrete failure. The finite element model, using tetrahedral elements, and the algorithms for tracking the crack surfaces in 3D, were implemented within the multi-purpose finite element software FEAP. The implementation is based on an user-defined macro and an external software package, developed by the authors, which handles the representation and progress of 3D cracks.

The PUFEM formulation, when used in combination with the proposed two-step algorithm, leads to a fast and robust tracking of 3D crack paths. This was aimed to be illustrated by means of two representative numerical examples, i.e. the simulation of the *Nooru-Mohamed test* and the *Brokenshire test*, using completely unstructured tetrahedral finite meshes. The analyses were based on geometrical, constitutive, loading and boundary-value data adopted from the literature. The obtained numerical results are in good agreement with experimental data, and are compared and discussed with respect to other published numerical analyses. The presented approach is well-suited for modeling 3D crack propagation in unreinforced concrete, with the only limitation that intersecting cracks can not be captured yet. An extension to intersecting cracks is desirable, however, most probably accompanied by serious topological complexities for general 3D applications.

## Acknowledgement

Financial support for this research was provided by the *Austrian Science Foundation* under *START-Award Y74-TEC*. This support is gratefully acknowledged.

## Appendix A

The solution of the minimization problem, as given in (15), reduces to the solution of the optimality conditions $\partial\Phi/\partial a_i = 0$, $i = 0,\ldots,5$ (where $i = 0,\ldots,2$ is for the case that the surface is described by a linear function). That leads to a symmetric (and real) system of linear equations

$$\sum_{i=1}^{n_{R^\star}} \left[\begin{array}{ccc|ccc} 1 & \overline{X}_i & \overline{Y}_i & \overline{X}_i^2 & \overline{Y}_i^2 & \overline{X}_i\overline{Y}_i \\ & \overline{X}_i^2 & \overline{X}_i\overline{Y}_i & \overline{X}_i^3 & \overline{X}_i\overline{Y}_i^2 & \overline{X}_i^2\overline{Y}_i \\ & & \overline{Y}_i^2 & \overline{X}_i^2\overline{Y}_i & \overline{Y}_i^3 & \overline{X}_i\overline{Y}_i^2 \\ \hline & & & \overline{X}_i^4 & \overline{X}_i^2\overline{Y}_i^2 & \overline{X}_i^3\overline{Y}_i \\ & \text{sym.} & & & \overline{Y}_i^4 & \overline{X}_i\overline{Y}_i^3 \\ & & & & & \overline{X}_i^2\overline{Y}_i^2 \end{array}\right] \left[\begin{array}{c} a_0 \\ a_1 \\ a_2 \\ \hline a_3 \\ a_4 \\ a_5 \end{array}\right] = \sum_{i=1}^{n_{R^\star}} \left[\begin{array}{c} \overline{Z}_i \\ \overline{X}_i\overline{Z}_i \\ \overline{Y}_i\overline{Z}_i \\ \hline \overline{X}_i^2\overline{Z}_i \\ \overline{Y}_i^2\overline{Z}_i \\ \overline{X}_i\overline{Y}_i\overline{Z}_i \end{array}\right]$$

to be solved for the coefficients $a_0,\ldots,a_5$ (or $a_0,\ldots,a_2$), which is straightforward if enough (well-distributed) nodes $n_{R^\star}$ of the point cloud are available.

## References

[1] J.H. Argyris, G. Faust, K.J. Willam, Limit load analysis of thick-walled concrete structures—a finite element approach to fracture, Comput. Methods Appl. Mech. Engrg. 8 (1976) 215–243.

[2] F. Armero, K. Garikipati, Recent advances in the analysis and numerical simulation of strain localization in inelastic solids, in: D.R.J. Owen, E. Oñate (Eds.), Computational Plasticity: Fundamentals and Applications. Proceedings of the Fourth International Conference, Pineridge press, Barcelona, 1995, pp. 547–561.

[3] F. Armero, K. Garikipati, An analysis of strong discontinuities in multiplicative finite strain plasticity and their relation with the numerical simulation of strain localization in solids, Int. J. Solids Struct. 33 (1996) 2863–2885.

[4] G.I. Barenblatt, The mathematical theory of equilibrium of cracks in brittle fracture, Adv. Appl. Mech. 7 (1962) 55–129.
[5] Z.P. Bažant, Concrete fracture models: testing and practice, Engrg. Fract. Mech. 69 (2002) 165–205.
[6] Z.P. Bažant, G. Pijaudier-Cabot, Nonlocal continuum damage, localization instability and convergence, J. Appl. Mech. 55 (1988) 287–293.
[7] T. Belytschko, J. Fish, A. Engelmann, A finite element with embedded localization zones, Comput. Methods Appl. Mech. Engrg. 70 (1988) 59–89.
[8] D. Bigoni, D. Zaccaria, On the eigenvalues of the accustic tensor in elastoplasticity, Eur. J. Mech. A/Solids 13 (1994) 621–638.
[9] D.R. Brokenshire, Torsional fracture tests. PhD thesis, Cardiff University, UK, 1996.
[10] B.D. Coleman, W. Noll, The thermodynamics of elastic materials with heat conduction and viscosity, Arch. Ration. Mech. Anal. 13 (1963) 167–178.
[11] D.S. Dugdale, Yielding of steel sheets containing slits, J. Mech. Phys. Solids 8 (1960) 100–104.
[12] T.C. Gasser, G.A. Holzapfel, Geometrically non-linear and consistently linearized embedded strong discontinuity models for 3D problems with an application to the dissection analysis of soft biological tissues, Comput. Methods Appl. Mech. Engrg. 192 (2003) 5059–5098.
[13] T.C. Gasser, G.A. Holzapfel, Modeling crack 3D propagation in unreinforced concrete using PUFEM, Comput. Methods Appl. Mech. Engrg. 194 (2005) 2859–2896.
[14] A. Hillerborg, M. Modeer, P.E. Petersson, Analysis of crack formation and crack growth in concrete by means of fracture mechanics and finite elements, Cement Concrete Res. 6 (1976) 773–782.
[15] G.A. Holzapfel, Nonlinear Solid Mechanics. A Continuum Approach for Engineering, John Wiley & Sons, Chichester, 2000.
[16] A.D. Jefferson, CRAFT—a plastic–damage-contact model for concrete. I. Model theory and thermodynamic considerations, Int. J. Solids Struct. 40 (2003) 5973–5999.
[17] A.D. Jefferson, CRAFT—a plastic–damage-contact model for concrete. II. Model implementation with implicit return-mapping algorithm and consistent tangent matrix, Int. J. Solids Struct. 40 (2003) 6001–6022.
[18] A.D. Jefferson, B.I.G. Barr, T. Bennet, S.C. Hee, Three dimensional finite element analysis of fracture tests using the CRAFT concrete model, Comput. Concrete 1 (2004) 261–284.
[19] M. Jirásek, Comparative study on finite elements with embedded discontinuities, Comput. Methods Appl. Mech. Engrg. 188 (2000) 307–330.
[20] C.E. Kesler, D.J. Naus, J.L. Lott, Fracture mechanics—its applicability to concrete, in: Proceedings of the International Conference on the Mechanical Behavior of Materials, Kyoto 1971, The Society of Material Sciences, 1972, pp. 113–124.
[21] J. Mandel, Conditions de stabilié et postulat de Drucker, in: J. Kravtchenko, P.M. Sirieys, (Eds.), Rheology and Soil Mechanics, Berlin, Germany, 1966, pp. 58–68.
[22] R. de Borst, Some recent developments in computational modelling of concrete fracture, Int. J. Fracture 86 (1997) 5–36.
[23] R. de Borst, Some recent issues in computational failure mechanics, Int. J. Numer. Methods Engrg. 52 (2001) 63–95.
[24] R. de Borst, L.J. Sluys, H.B. Hüllhaus, J. Pamin, Fundamental issues in finite element analysis of localization of deformation, Engrg. Comput. 10 (1993) 99–121.
[25] J.M. Melenk, I. Babuška, The partition of unity finite element method: basic theory and applications, Comput. Methods Appl. Mech. Engrg. 139 (1996) 289–314.
[26] N. Moës, A. Gravouil, T. Belytschko, Non-planar 3D crack growth by the extended finite element and level sets—Part I: mechanical model, Int. J. Numer. Methods Engrg. 53 (2002) 2549–2568.
[27] A. Needleman, A continuum model for void nucleation by inclusion debonding, J. Appl. Mech. 54 (1987) 525–531.
[28] A. Needleman, An analysis of decohesion along an imperfect interface, Int. J. Fracture 42 (1990) 21–40.
[29] M.B. Nooru-Mohamed, Mixed-mode fracture of concrete: an experimental approach, PhD thesis, Delft University of Technology, The Netherlands, 1992.
[30] R.W. Ogden, Non-linear Elastic Deformations, Dover, New York, 1997.
[31] J. Oliver, Continuum modelling of strong discontinuities in solid mechanics, in: D.R.J. Owen, E. Oñate (Eds.), Computational Plasticity: Fundamentals and Applications. Proceedings of the Fourth International Conference, Pineridge press, Barcelona, 1995, pp. 455–479.
[32] J. Oliver, On the discrete constitutive models induced by strong discontinuity kinematics and continuum constitutive equations, Int. J. Solids Struct. 37 (2000) 7207–7229.
[33] J. Oliver, M. Cervera, O. Manzoli, Strong discontinuities and continuum plasticity models: the strong discontinuity approach, Int. J. Plasticity 15 (1999) 319–351.
[34] J. Oliver, A.E. Huespe, E. Samaniego, E.W.V. Chaves, On strategies for tracking strong discontinuities in computational failure mechanics, in: H.A. Mang, F.G. Rammerstorfer, J. Eberhardsteiner (Eds.), Proceedings of the Fifth World Congress on Computational Mechanics (WCCM V), Vienna University of Technology, Vienna, Austria, 2002.
[35] J. Oliver, A.E. Huespe, E. Samaniego, E.W.V. Chaves, Continuum approach to the numerical simulation of material failure in concrete, Int. J. Numer. Anal. Methods Geomech. 28 (2004) 609–632.
[36] J. Oliver, A.E. Huespe, M.D.G. Pulido, E. Chaves, From continuum mechanics to fracture mechanics: the strong discontinuity approach, Engrg. Fract. Mech. 69 (2002) 113–136.
[37] M. Ortiz, Y. Leroy, A. Needleman, A finite element method for localized failure analysis, Comput. Methods Appl. Mech. Engrg. 61 (1987) 189–214.
[38] S. Osher, J.A. Sethina, Fronts propagating with curvature depending speed: algorithms based on Hamilton–Jacobi formulations, J. Comput. Phys. 79 (1988) 12–49.
[39] B. Patzák, M. Jirásek, Adaptive resolution of localized damage in quasibrittle materials, J. Engrg. Mech. 130 (2004) 720–732.
[40] P. Pivonka, J. Ožbolt, R. Lackner, H.A. Mang, Comparative studies of 3D-constitutive models for concrete: application to mixed-mode fracture, Int. J. Numer. Methods Engrg. 60 (2004) 549–570.
[41] J.G. Rots, Computational modeling of concrete fracture, PhD thesis, Delft University of Technology, Netherlands, 1988.
[42] J.W. Rudnicki, J.R. Rice, Conditions for the localization of deformation in pressure-sensitive dilatant materials, J. Mech. Phys. Solids 23 (1975) 371–394.
[43] J. Schöberl, NETGEN—A 3D Tetrahedral Mesh Generator—Version 4.2, University Linz, Austria, 2002.
[44] J.C. Simo, J. Oliver, A new approach to the analysis and simulation of strain softening in solids, in: Z.P. Bažant, Z. Bittnar, M. Jirásek, J. Mazars (Eds.), Fracture and Damage in Quasibrittle Structures: Proceedings of the US–Europe Workshop on Fracture and Damage in Quasibrittle Structures, E&FN Spon, London, 1994, pp. 25–39.
[45] J.C. Simo, M.S. Rifai, A class of mixed assumed strain methods and the method of incompatible modes, Int. J. Numer. Methods Engrg. 29 (1990) 1595–1638.
[46] A. Simone, H. Askes, L.J. Sluys, Incorrect initiation and propagation of failure in non-local and gradient-enhanced media, Int. J. Solids Struct. 41 (2004) 351–363.

[47] L.J. Sluys, A.H. Berends, Discontinuous failure analysis for mode-I and mode-II localization problems, Int. J. Solids Struct. 35 (1998) 4257–4274.
[48] A.J.M. Spencer, Constitutive theory for strongly anisotropic solids, in: A.J.M. Spencer (Ed.), Continuum Theory of the Mechanics of Fibre-Reinforced Composites, CISM Courses and Lectures No. 282, Springer-Verlag, Wien, 1984, pp. 1–32, International Centre for Mechanical Sciences.
[49] P. Steinmann, R. Larsson, K. Runesson, On the localization properties of multiplicative hyperelasto-plastic continua with strong discontinuities, Int. J. Solids Struct. 34 (1997) 969–990.
[50] M. Stolarska, D.L. Chopp, N. Moës, T. Belytschko, Modelling crack growth by level sets in the extended finite element method, Int. J. Numer. Methods Engrg. 51 (2001) 943–960.
[51] R.L. Taylor, FEAP—A Finite Element Analysis Program—Version 7.3, University of California, Berkeley, 2000.
[52] V. Tvergaard, J.W. Hutchinson, The relation between crack growth resistance and fracture process parameters in elastic–plastic solids, J. Mech. Phys. Solids 40 (1992) 1377–1397.
[53] A.G. Varias, N.P. O'Dowd, R.J. Asaro, C.F. Shih, Failure of bimaterial interfaces, Mater. Sci. Engrg. A 126 (1990) 65–93.
[54] G. Ventura, E. Budyn, T. Belytschko, Vector level sets for description of propagating cracks in finite elements, Int. J. Numer. Methods Engrg. 58 (2003) 1571–1592.
[55] G.N. Wells, Discontinuous modelling of strain localization and failure, PhD thesis, Delft University of Technology, Netherlands, 2001.
[56] G.N. Wells, R. de Borst, L.J. Sluys, A consistent geometrically non-linear approach for delamination, Int. J. Numer. Methods Engrg. 54 (2002) 1333–1355.
[57] O.C. Zienkiewicz, R.L. Taylor, The Finite Element Method, fifth ed. The Basis, vol. 1, Butterworth Heinemann, Oxford, 2000.